# THE DEPENDENCE ON INITIAL BEAM CONDITIONS OF THE PROPAGATION OF ULTRASHORT LASER PULSES

A Dissertation

Presented to the Faculty of the Graduate School

of Cornell University

in Partial Fulfillment of the Requirements for the Degree of

Doctor of Philosophy

by

Samuel Schrauth

January 2015

# THE DEPENDENCE ON INITIAL BEAM CONDITIONS OF THE PROPAGATION OF ULTRASHORT LASER PULSES

Samuel Schrauth, Ph. D.

Cornell University 2015

This thesis presents the nonlinear propagation dynamics in isotropic media. The influence of initial conditions on the propagation dynamics is considered. Three different instances are considered. We experimentally and numerically study the influence the temporal profile of a laser pulse has on the propagation and collapse dynamics when propagating in different group velocity dispersion regimes. We are interested in the spatio-temporal collapse dynamics of super-Gaussian pulses in this regime. We find that with a super-Gaussian pulse, we see pulse-splitting in this regime. We numerically study how the transverse beam profile effects the propagation in waveguide structures, both step-index fibers and hollow metallic waveguides. We are interested in modes that are necklace beams, with the possibility of application for high-power fiber lasers and amplifiers. We find that there is a benefit in the power threshold for collapse, but that is depends strongly on exciting the desired mode. Finally, we experimentally study the propagation of high power beams, which interact due to the Kerr nonlinearity. The main interest is in the propagation under conditions in which they exhibit spiral motion. We see large rotation of about 40 degrees when the collapsing beams are interacting.

## BIOGRAPHICAL SKETCH

The author was born in Ohio to Peter and Christine Schrauth. He grew up as the third of four children in Elmira, NY. From a young age he always had an interest in math and science. He attended Elmira Free Academy and graduated in June of 2002. That fall, he entered the University of Rochester intending to study physics. After discovering that the University of Rochester had a department devoted entirely to optics, The Institute of Optics, he knew what he wanted to study. In addition to standard classes during the academic year, his education was supplemented with interesting and illuminating research activities over the summers. He was a summer student at the Laboratory for Laser Energetics the summer of 2004. The summer of 2005 he was a National Science Foundation REU student at Cornell. He graduated from the University of Rochester with a BS in Optics in May of 2006. The summer after graduating was spent at Lawrence Livermore National Laboratory as a summer student. The next step in his education was to enter the Applied Physics Ph.D. program at Cornell University in the fall of 2006.

To my family and my puzzle piece

# ACKNOWLEDGMENTS

I want to thank Professor Alexander Gaeta for allowing me to be a part of his research group. It was not always easy, but I was surrounded by many fellow graduate students and post-docs that helped me get through it. So, to the past and present members of the Gaeta group that I have overlapped with, I want to say "Thank you!" I especially want to thank Dr. Bonggu Shim, not only for teaching me and helping me to develop as a researcher, but genuinely taking an interest in what I was doing and what was going on in my life. You have been invaluable to my development and I cannot say thank you enough.

I am also grateful to those people outside of the research group that helped to take my mind off of the lab for a bit. This was invaluable when frustration was staring to set in. Having the running group made Saturday morning runs and breakfasts one of my favorite parts of some difficult weeks, especially towards the end of my time in Ithaca. In addition, being a part time swim coach helped to keep a foot on the ground, or a body in the pool.

Finally, I want to thank my family. They have supported me through thick and thin, the good and the bad, the easy and the hard, and were always there when I needed you. I consider myself lucky to have such a support group.

TABLE OF CONTENTS

LIST OF FIGURES

# CHAPTER 1

# INTRODUCTION

With the invention of the laser [1], the electric field strengths needed to observe the nonlinear response of materials became available to researchers. The response is nonlinear in the sense that the field strength changes how a material responds. The first optical nonlinearity discovered was second-harmonic generation, where there is a response at double the frequency of the driving laser [2].

Other optical nonlinearities were discovered and studied such as the intensity-dependent refractive index, often referred to as the optical Kerr effect [3]. This effect is described as the presence of a strong electric field that causes a change in the local refractive index of the material. A result of the intensity-dependent refractive index is that high power laser beams can create a gradient index profile, which acts as a lens. This effect is termed *self-focusing*, since the presence of the beam will cause a change in the refractive index and this causes the beam to focus. In addition there was found to be a critical power, above which there will be collapse of the self-focusing beam [4]. This power was determined to be the power contained in the Townes profile, which is a solution to the nonlinear Schrödinger equation. The study of laser beam propagation with powers near and above the critical power continues to be an active research area to this day.

The most fundamental equations for working with classical electrodynamics are Maxwell's equations. This set of four coupled differential equations governs the propagation of electromagnetic fields, which includes lasers. Maxwell's equations are:

$$\nabla \times \mathbf{E} = -\frac{1}{c}\frac{\partial \mathbf{B}}{\partial t} \quad \nabla \times \mathbf{H} = \frac{1}{c}\frac{\partial \mathbf{D}}{\partial t} + \frac{4\pi}{c}\mathbf{J}, \qquad (1.1)$$
$$\nabla \cdot \mathbf{D} = 4\pi\rho \qquad \nabla \cdot \mathbf{B} = 0$$

where **E** is the electric field, **B** is the magnetic induction, **D** is the electric displacement field, and **H** is the magnetic intensity. **J** and ρ are the current density and free charge density respectively. The speed of light is c. The relationship between the pairs of electric and magnetic vectors are the constitutive relations, which are:

$$\mathbf{D} = \mathbf{E} + 4\pi\mathbf{P} \quad \mathbf{H} = \mathbf{B} - 4\pi\mathbf{M}, \qquad (1.2)$$

where **P** is the polarization and **M** is the magnetization. Again, these are vector quantities and they are dependent on the material, such as an optical glass, through which the electromagnetic field is propagating.

The origin of the material nonlinearity is contained in Maxwell's equations but hidden in the constitutive relations. The origin of the intensity-dependent refractive index can be explained using perturbative nonlinear optics. This framework is valid when the electric field is large enough to result in a nonlinear material response, but not large enough to significantly alter the electric potential of the material the beam is propagating through. For this regime, the polarization can be expanded in a power series of the electric field,

$$P = \chi^{(1)}E + \chi^{(2)}E^2 + \chi^{(3)}E^3 + \ldots, \qquad (1.3)$$

where $E$ is the electric field, $\chi^{(1)}$ is the linear susceptibility and responsible for the linear refractive index, $n_0$. $\chi^{(2)}$ is the second-order nonlinear susceptibility and is responsible for effects such as second-harmonic generation, sum-frequency generation, and difference-frequency generation [3]. $\chi^{(3)}$ is the third-order nonlinear susceptibility and is responsible for effects such as self-phase modulation, third-harmonic generation, and four-wave mixing among others [3]. In

writing the material polarization in the form of equation 1.3, we have neglected the vector nature of the polarization and electric fields and the tensor nature of the susceptibilities.

Here, we are interested in the self-focusing of high-power laser beams and pulses due to the intensity-dependent index, which is a result of the third-order optical nonlinearity. The reason we can neglect the second-order nonlinearity is that for centrosymmetric (defined as having inversion symmetry) materials, such as glass, water, and gases, this term in the expansion must disappear due to symmetry arguments. This leaves the third-order nonlinearity as the lowest order term in the expansion of the polarization for centrosymmetric materials.

For third-order nonlinearities, such as four-wave mixing and third-harmonic generation, a phase-matching condition is required for an efficient nonlinear process. Since the intensity-dependent refractive index is not converting the frequency of the light, phase-matching is not required. The third order susceptibility is related to the intensity-dependent refractive index by the expression

$$n_2 = \frac{3}{4n_0^2 \varepsilon_0 c} \chi^{(3)}, \tag{1.4}$$

where $n_0$ is the linear refractive index, $c$ is the speed of light and $\varepsilon_0$ is the permittivity of free space. Considering this nonlinearity, the refractive index profile of a material due to an intense laser beam can be written as

$$n(r) = n_0 + n_2 I(r), \tag{1.5}$$

where $I(r)$ is the radial intensity profile of the beam. This expression describes a gradient index caused by the presence of the high-intensity beam. The majority of materials have a positive value of $n_2$ at the optical wavelengths.

As an example of the result of the intensity dependent index, we can look at a common optical glass, BK7, with values of $n_0$=1.51 and $n_2$=3.2x10$^{-16}$ cm$^2$/W. For a beam that has a spot size of 100 μm and power of 2 MW we can calculate the intensity profile and the refractive index profile that results from the intensity-dependent refractive index. These are shown in Figure 1.1.

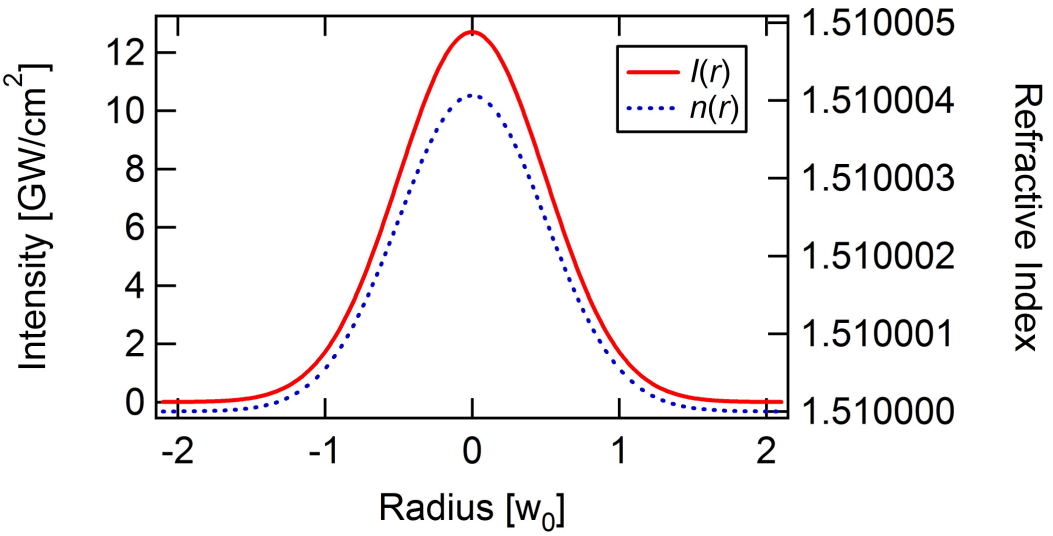


Figure 1.1 The intensity profile, $I(r)$, of a 2 MW beam with a spot size of 100 μm and the resulting refractive index profile, $n(r)$, from the intensity-dependent refractive index.

As can be seen in Figure 1.1, the change in the refractive index by high-intensity beams between the peak of the beam and the edge of the beam is approximately $5\times10^{-6}$. This is a small amount and would not appear to have a large overall effect. However, this is only an instantaneous view of the beam intensity and the refractive index profile along propagation. The gradient index causes the material to act as a lens and focus the light. As the light focuses, the intensity will be grow larger, so there will be a slightly larger change in the refractive index and the gradient will result in a slightly stronger lens. The change in the beam profile and the corresponding change in the intensity profile that occurs with propagation must be taken into account.

In order to model the propagation of the beam and the changing intensity-dependent refractive index profile, we must use the nonlinear Schrödinger equation (NLSE). The derivation starts from Maxwell's equations, equations 1.1, and the constitutive relations, equations 1.2. The nonlinear polarization is assumed to be of the form of equation 1.3. The derivation of the NLSE is contained in standard nonlinear optics textbooks [3]. There are five assumptions made to get from Maxwell's equations to the NLSE: (1) there are no free charges, (2) the material is non-magnetic, (3) we neglect any vector and tensor effects, (4) the susceptibilities are nonresonant, and (5) the beam profile is a slowly varying envelope in space. After these assumptions, the electric field is written as $E(x,y)=A_0\psi(\eta, \xi)$ with $\psi$ being the normalized field. The Nonlinear Schrödinger equation is found to be

$$\frac{\partial \psi}{\partial \zeta} = \frac{i}{4}\nabla_{\perp}^{2}\psi + i\frac{L_{DF}}{L_{NL}}|\psi|^{2}\psi , \qquad (1.6)$$

where $w_0$ is the spot size, $L_{DF}=k\,w_0^2/2$ is the diffraction length, $L_{NL}=(n_2 n_0 \omega |A_0|^2/2\pi)^{-1}$ is the nonlinear length, $|A_0|$ is the magnitude of the input laser field, $\eta=x/w_0$ and $\xi$=y/ $w_0$ are the normalized coordinates, $\zeta=z/L_{DF}$ is the normalized propagation length. The left hand side of the equation is the propagation term. The first term, with the transverse laplacian on the right hand side of the equation accounts for diffraction and the second term with the ratio of $L_{DF}$ to $L_{NL}$ accounts for the self-focusing due to the intensity-dependent refractive index. This is the simplest form of the NLSE, neglecting temporal effects and taking into account only spatial effects. When electric field is larger, or the pulse very short, other terms must be added such as dispersion, self-steepening, ionization, and plasma defocusing terms [5]. When such effects are included, the study of self-focusing dovetails with the studies of filamentation of ultrashort laser pulses. A filament is the name given to the long distance propagation of a laser pulse due to the balance of diffraction, self-focusing, and plasma defocusing.

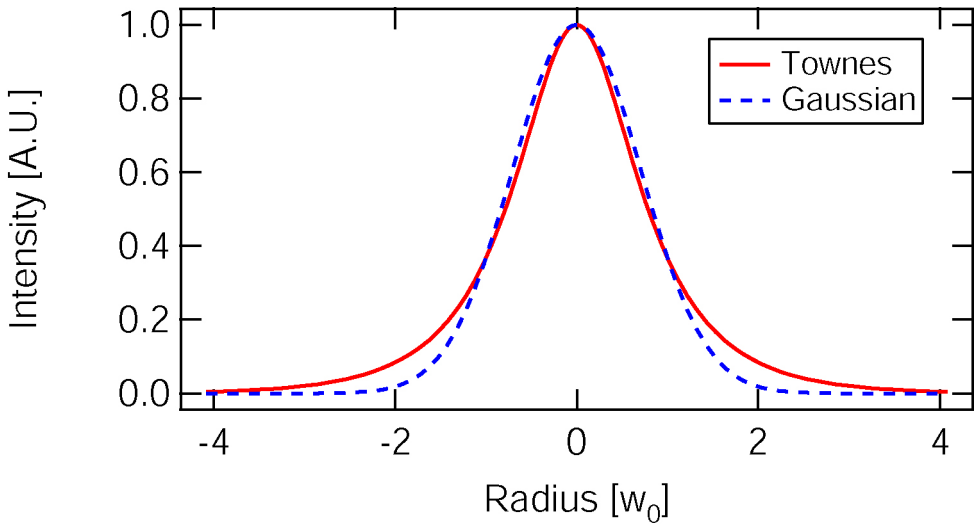


Figure 1.2 Comparison of the Townes profile, the solution to the spatial NLSE, to a Gaussian radial profile. The two profiles have the same 1/e radius.

A solution to the NLSE has been found as written in equation 1.6. It is found by looking for a waveguide solution, where the dependence on the propagation coordinate is just a phase factor. With this assumption, the left hand side of the equation 1.6 becomes zero and it is no longer a partial differential equation, but an ordinary differential equation in the radial coordinate. It still must be solved numerically though and the solution is the Townes profile [4]. The numerically calculated Townes profile is shown in Figure 1.2 along with a Gaussian profile. The beams are scaled such that they have the same 1/e radius. The two profiles look similar, but the Townes profile has more energy in the wings. The power of the Townes profile is the critical power for collapse, $P_{CR}$, and is the lower bound for which collapse will occur. The expression for the critical power is given by,

$$P_{CR} = \frac{\alpha\lambda^2}{4\pi n_0 n_2}, \qquad (1.7)$$

where $\lambda$ is the wavelength, $n_0$ is the linear refractive index, and $n_2$ is the nonlinear refractive index. The critical power is dependent on material properties like $n_0$ and $n_2$ and is on the order of

megawatts for optical glasses and gigawatts for gases at standard temperature and pressure. If the beam shape is changed, but remains radially symmetric, the threshold for collapse will be slightly higher and is taken into account in equation 1.7 by the shape dependent factor, $\alpha$. For the Townes, profile, the value of $\alpha$ is 1.86225 [6]. For the case of the optical glass BK7 stated before, the critical power for collapse at 800 nm is 1.96 MW. So even though the change in refractive index is approximately $5\times10^{-6}$ for the beam parameters stated, this small change can result in large effect when the change of the beam profile with propagation is included. For a beam with such parameters propagating through a nonlinear media, it will undergo self-focusing upon propagation and evolve from a Gaussian beam profile to the Townes profile.

The initial conditions, such as beam shape and power, can have an affect on the collapse dynamics. Since it is experimentally easy to generate beams with powers much greater than the critical power, it is valid to consider what happens for beams of such power levels. For example, a Gaussian beam that contains multiple critical power will certainly collapse. The way it collapses is the interesting part. It collapses such that the number of filaments is quantized and roughly equal to the number of critical powers contained in the beam [7]. The location of the collapse is seeded by the noise that is present in the initial beam profile. This sort of noise-seeded collapse can be altered though, with appropriate choice of the initial beam shape, for example, an elliptical beam. Changing the beam profile to an elliptical profile has a few interesting effects. Elliptical beams show an increase in the collapse threshold, with an increase in the ellipticity of the beam, but it is relatively weak. For example, an elliptical beam with and ellipticity of 5, is predicted to have a collapse threshold of approximately 2.6 $P_{CR}$ [8, 9]. In addition to this increase in the collapse threshold for the elliptical beam, there is also a difference when the power is the in the multiple filamentation regime. For beams with much more than a

critical power, the elliptical beam will collapse into multiple filaments, but the filaments will be in a line along the major axis of the beam, as opposed to being distributed over the entire beam profile seeded by noise [10-12]. So a change in beam shape from a radially symmetric Gaussian to a highly elliptical beam changes not only the power threshold for collapse, but also the multiple filamentation pattern.

In addition to highly elliptical beams, there have been studies into other beam profiles and types that can affect the propagation dynamics. As stated before and shown numerically, many beam shapes have collapse thresholds near $P_{CR}$ [6]. When the beam shape starts to diverge from a Gaussian, then the collapse dynamics can change dramatically, whether it is an increase in the collapse threshold or the beam profile to which it collapses. High-power super-Gaussian have been shown, both theoretically and experimentally, to undergo collapse and evolve through a ring solution, before collapsing to Townes profiles at the radius of the ring profile [13-15]. The number of Townes profiles depends on the number of critical powers that are contained in the initial beam. Another beam profile that has been studied both theoretically and experimentally in bulk is the necklace beam [16-18]. A necklace beam is a beam profile that has off-axis beads at an off-axis radius. The neighbors for anyone bead are $\pi$ out-of-phase with the neighbors. Necklace beams showed a collapse threshold that was approximately equal to the number of beads in the profile. There has also been work on beams that have some sort of vorticity to them, whether they are optical vortices [19] or polarization vortices [20]. The optical vortices look like a ring profile, but have a helical phase. The polarization vortices also look like a ring profile, but polarization direction of the electric field changes depending on the position in the beam profile. Both of these profiles show a higher collapse threshold as well as collapsing to Townes profiles at the radius of the ring. As can be seen from the previous theoretical and

experimental work, beam shape can have a definite effect on the propagation dynamics and the collapse threshold.

In addition to altering the beam shape, altering the phase across the beam also changes the self-focusing dynamics, but not necessarily the collapse threshold. The simplest case is a collimated beam propagating through the Kerr media. The self-focusing distance is well known. If the beam profile has a varying phase, for example, from passing through a single lens, then the self-focusing distance can be altered [3]. There have been experiments that have shown how an altering the phase across a beam can have such affect. The use of a simple two-lens setup can change the collapse distance as well as the filament length [21]. Such simple things as changing the phase on a beam profile can certainly affect the self-focusing dynamics and filament formation.

Changing the initial conditions of beam before nonlinear propagation can certainly have affects on the propagation of the laser through a nonlinear medium. We explore how changing the initial pulse shape effects the propagation. In addition we look at how higher-order modes propagating in fibers behave differently for high powers. Finally, we look at the propagation of interacting beams, with slightly different propagation directions, in water.

### *1.1 Super-Gaussian pulses in the anomalous GVD regime*

When looking at the propagation of ultrashort pulses in a nonlinear medium, the simple NLSE will not be sufficient to describe the propagation dynamics. In this case, group-velocity dispersion (GVD) must be included. The value and sign of the GVD will affect the propagation dynamics. For much of the work looking at the spatio-temporal propagation, the input pulse was either a Gaussian or sech-squared pulse. This is due to the fact that altering the pulse shape is more complicated experimentally then changing the spatial profile of a beam. Of interest was

how the initial pulse-shape, coupled with the sign of the GVD would change the propagation dynamics.

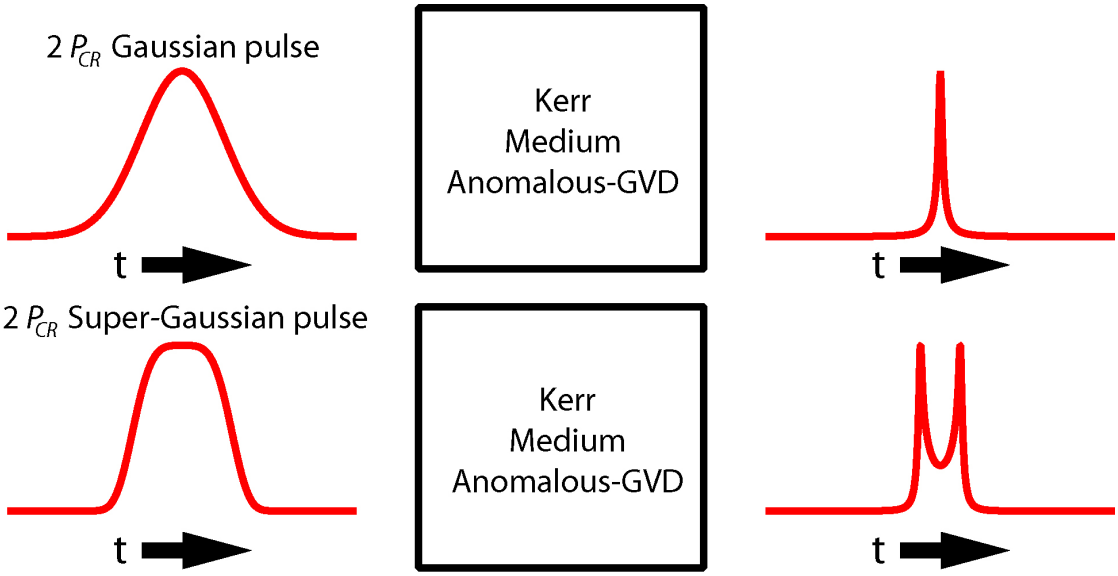


Figure 1.3 Schematic of the pulse-splitting experiment. The high-power pulses propagate though a Kerr medium in the anomalous group-velocity dispersion regime and undergo spatio-temporal collapse. The temporal profile of the collapsing beam depends on the input pulse shape. For a Gaussian input spatio-temporal collapse is expected. For the super-Gaussian input, we see pulse-splitting which was not previous seen.

Based on work done looking at the collapse of super-Gaussian beams [15], there was interest in how a super-Gaussian pulse would collapse, specifically when propagating in the anomalous GVD regime.

We find that in this regime, the super-Gaussian undergoes pulse-splitting as it collapses. This is in contrast to the Gaussian beam in the anomalous GVD regime, which undergoes spatio-temporal collapse. This opens up the possibility of using the pulse-shape to control collapse dynamics.

### *1.2 Higher-order modes in step-index waveguides*

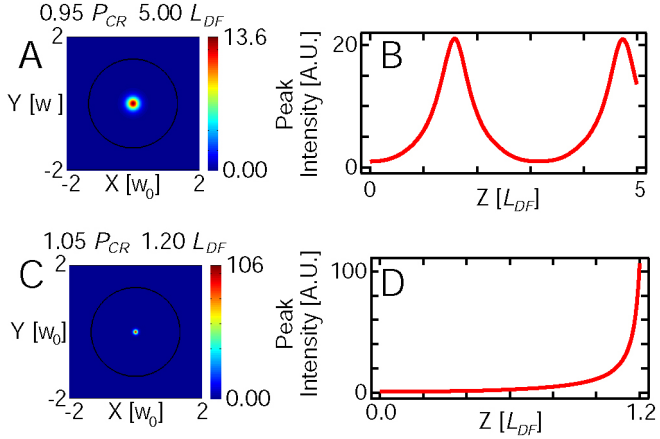


Figure 1.4 Propagation of the fundamental $LP_{01}$ mode in a step index waveguide. A. The output mode for the propagation of high-power mode with 0.95 $P_{CR}$. B. Is the peak intensity for that input power. C. The collapsed output for propagation of high-power mode with 1.05 $P_{CR}$. D. Is the peak intensity for that input power. For the propagation of a beam with power less than $P_{CR}$, self-focusing does occur, but it results in oscillations of the peak intensity, but no collapse. For the case of a beam propagating with more than one $P_{CR}$, we see the collapse that is expected.

Much like the studies of the propagation of lasers in bulk materials, there has been work looking into the high-power propagation in designed waveguides. A large amount of this work has been focused on the design and development of large mode-area fiber for use in fiber lasers [22] or fiber amplifiers [23]. These higher-order modes had been radially symmetric, with a high field in the center and then oscillations as the radial coordinate increases. A separate study looked at how a fiber with a low index region in the center of the core would change the high-power propagation dynamics [24]. In addition to cylindrically symmetric fibers, there has also been work on looking into rectangular core waveguides to explore high power propagation [25, 26]. All of these studies have involved the design of a waveguide structure, which can be involved, especially the effort that goes into producing the waveguide.

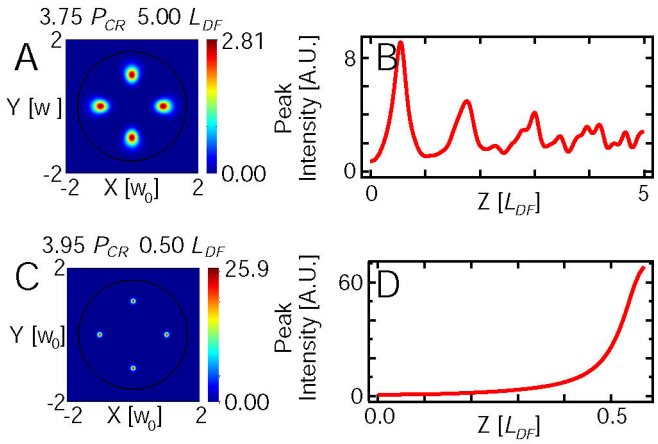


Figure 1.5 Propagation of the Higher-order $LP_{21}$ mode in a step index waveguide. A. The output mode for the propagation of high-power mode with 3.75 $P_{CR}$. B. Is the peak intensity for that input power. C. The collapsed output for propagation of high-power mode with 3.95 $P_{CR}$. D. Is the peak intensity for that input power. We see increased resistance to collapse when the input mode has a beaded structure. The fiber can transmit more than $P_{CR}$.

We numerically investigate the propagation of a specific class of higher-order modes, which are not radially symmetric, in standard step-index fiber and hollow metallic waveguides. We are interested in the $LP_{v1}$ modes, which are very similar to the necklace beams studied experimentally in the bulk [18]. The expectation is that there would be some benefit from the propagation of these necklace beams in the standard waveguides, without the need to design and produce a custom waveguide structure.

We find that, for the distances studied, we observe an increase of the collapse threshold and the propagation distance for both the step-index and hollow metallic waveguide. Figure 1.4 shows the propagation of the fundamental mode of a step-index fiber. We see that collapse occurs at the same value as in bulk, than $P_{CR}$. Compare this to the propagation of the $LP_{21}$ mode shown in figure 1.5, where a beam with 3.75 $P_{CR}$ propagates without collapsing, while the mode with 3.95 $P_{CR}$ does collapse. We also look at the importance of the mode shape being unperturbed and find it is quite important in order to obtain this benefit.

### *1.3 Spiral motion of collapsing beams in water*

Another interesting case where the initial condition can change the propagation dynamics of the high-power laser beam is when there are two beams propagating in the roughly the same

direction. Depending on the phase relationship of the beams, there can be interesting interactions that take place between the high-power, collapsing, and propagating beams.

There has been much work focused on the interactions of solitons [27]. The behavior has spanned a ride range of interactions. There has been the study of long-range interactions between solitons [28]. The energy transfer between solitons with a $\pi/2$ phase relationship was also studied, with the ability to switch which soliton would acquire the energy by switching which soliton was phase-advanced [29]. The interaction was also investigated in quadratic nonlinear material as opposed to third-order media where the interaction is due to the Kerr effect [30]. Scattering and spiraling where shown in that specific experiment. Interacting solitons were also shown to exhibit three-dimensional spiraling [31]. These interactions dependent on the phase relationship between solitons have been experimentally demonstrated before.

All of this work has been done looking at spatial solitions. The study of interacting collapsing beams and filaments under similar conditions is also an active research topic. It has been shown experimentally in glass that two collapsing beams propagating in the same direction, but with spatial separation can exhibit behavior similar to that of solitons. The collapsing beams interact and can attract, repel, fuse, or share energy all depending on the initial separation and phase-relationship between the two beams [32]. The interaction of collapsing beams and filaments has also been numerically studied for high-power beams in air, showing the same interactions as were with collapsing beams in glass, attraction, repulsions, fusion, energy transfer, and additionally rotation [33]. These interactions of collapsing beams in air have been shown experimentally as well, with all of the expected interactions shown [34].

Here we look at the propagation of coupled, collapsing, optical beams with slightly different propagation directions in water. The phase difference between the beams is controlled so we can achieve the desired interactions. The beams are offset in the vertical and horizontal from each other, with a small crossing angle in the horizontal direction, but not the vertical direction. The water cell allows us to get a better idea of the evolution of the propagation for

different distances, in addition to the critical power being at a lower value than in a gaseous medium.

REFERENCES


1. T. H. Maiman, "Stimulated Optical Radiation in Ruby," Nature **187**, 493-494 (1960).

2. P. Franken, A. E. Hill, C. W. Peters, and G. Weinrich, "Generation of Optical Harmonics," Phys. Rev. Lett. **7**, 118-11 (1961).

3. R. Boyd, *Nonlinear Optics* (Academic Press, 2008).

4. R. Y. Chiao, E. Garmire, and C. H. Townes, "Self-Trapping of Optical Beams," Phys. Rev. Lett. **13**, 479-482 (1964).

5. A. Couairon and A. Mysyrowicz, "Femtosecond filamentation in transparent media," Phys. Rep. **441**, 47-189 (2007).

6. G. Fibich and A. Gaeta, "Critical power for self-focusing in bulk media and hollow waveguides," Opt. Lett. **25**, 335-337 (2000).

7. A. Braun, G. Korn, X. Liu, D. Du, J. Squier, and G. Mourou, "Self-channeling of high-peak power femtosecond laser pulses in air," Opt. Lett. **20**, 73-75 (1995).

8. C.R. Giuliano, J.H. Marburger, and A. Yariv, "Enhancement of the self-focusing threshold in sapphire with elliptical beams," Appl. Phys. Lett **21**, 58-60 (1967).

9. G.Fibch and B. Ilan, "Self-focusing of elliptical beams: an example of the failure of the aberrationless approximation," J. Opt. Soc. Am. B **17**, 1749-1758 (2000).

10. G. Fibich, S. Eisenmann, B. Ilan, and A. Zigler, "Control of multiple filamentation in air," Opt. Lett. **29**, 1772-1774 (2004).

11. T.D. Grow and A.L. Gaeta, "Dependence of multiple filamentation on beam ellipticity," Opt. Express **13**, 4594-4599 (2005).

12. B. Shim, S.E. Schrauth, L.T. Vuong, Y. Okawachi, and A.L. Gaeta, "Dynamics of elliptical beams in the anomalous group-velocity dispersion regime," Opt. Express **19**, 9139-9146 (2011).

13. G. Fibich, N. Gavish, and X. Wang, "Singular ring solutions of critical and supercritical nonlinear Schrodinger equations," Physica D **231**, 55-86 (2007).

14. N. Gavish, G. Fibich, L.T. Vuong, and A.L. Gaeta, "Predicting the filamentation of high-power beams and pulses without numerical integration: A nonlinear geometrical optics method," Phys. Rev. A **78**, 043807 (2008).

15. T.D. Grow, A.A. Ishaaya, L.T. Vuong, A.L. Gaeta, N. Gavish, and G. Fibich, "Collapse dynamics of super-Gaussian beams," Opt. Exp. **14**, 5468-5475 (2006).

16. M. Soljačić and M. Segev, "Self-trapping of "Necklace Beams" in Self-Focusing Kerr Media," Phys. Rev. Lett. **81**, 4851-4854 (1998).

17. M. Soljačić and M. Segev, "Self-trapping of "necklace-ring" beams in self-focusing Kerr media," Phys. Rev. E **62**, 2810-2820 (2000).

18. T.D. Grow, A.A. Ishaaya, L.T. Vuong, and A.L. Gaeta, "Collapse and Stability of Necklace Beams in Kerr Media," Phys. Rev. Lett. **99**, 133902 (2007).

19. L.T. Vuong, T.D. Grow, A. Ishaaya, A.L. Gaeta, G.W. 't Hooft, E.R. Eliel, and G. Fibich, "Collapse of Optical Vortices," Phys. Rev. Lett. **96**, 133901 (2006).

20. A.A. Ishaaya, L.T. Vuong, T.D. Grow, and A.L. Gaeta, "Self-focusing dynamics of polarization vortices in Kerr media," Opt. Lett. **33**, 13-15 (2008).

21. G. Fibich, Y. Sivan, Y. Ehrlich, E. Louzon, M. Fraenkel, S. Eisenmann, and A. Zigler, "Control of collapse distance in atmospheric propagation," Opt. Express **14**, 4946-4957 (2006).

22. S. Ramachandran, J.M. Fini, M. Mermelstein, J.W. Nicholson, S. Ghalmi, and M.F. Yan, "Ultra-large effective area, higher-order mode fibers: a new strategy for high-power lasers," Laser&Photon. Rev. **2**, 429-448 (2008).

23. J.W. Nicholson, J.M. Fini, A.M. Desantolo, X. Liu, K. Feder, P.S. Westbrook, V.R. Supradeepa, E. Monberg, F. DiMarcello, R. Ortiz, C. Headley, and D.J. DiGiovanni, "Scaling the effective area of higher-order-mode erbium-doped fiber amplifiers," Opt. Express **20**, 24575-24584 (2012).

24. A.D. Yablon and J. Jasapara, "Fiber designs for exceeding the bulk-media self-focusing threshold," Proc. SPIE **6543**, 64531D (2007).

25. D.A. Rockwell, V. Shkunov, and J.R. Marciante, "Semi-guiding high-aspect ratio core (SHARC) fiber providing single-mode operation and an ultra-large core area in a compact coilable package," Opt. Express **19**, 14746-14762 (2011).

26. D. Drachenberg, M. Messerly, P. Pax, A. Sridharan, J. Tassano and J. Dawson, "First multi-watt fiber oscillator in a high order mode," Opt. Express **21**, 18089-18096 (2013).

27. G.I Steeman and M. Segev, "Optical Spatial Solitons and Their Interactions: Universality and Diversity," Science **286,** 1518-1522 (1999).

28. C. Rotschild, B. Alfassi, O. Coehn, and M. Segev, "Long-range interactions between optical solitons," Nat. Photonics **2,** 769-774 (2006).

29. M. Shalaby, F. Reynaud, and A. Barthelemy, "Experimental observation of spatial soliton interactions with a π/2 relative phase difference," Opt. Lett. **17,** 778-780 (1992).

30. V.V. Steblina, Y.S. Kivshar, and A.V. Buryak, "Scattering and spiraling of solitons in a bulk quadratic medium," Opt. Lett. **23,** 156-158 (1998).

31. M. Shih, M. Segev, and G. Salamo, "Three-Dimensional Spiraling of Interacting Spatial Solitons," Phys. Rev. Lett. **78,** 2551-2554 (1997).

32. A.A. Ishaaya, T.D. Grow, S. Ghosh, L.T. Vuong, and A.L. Gaeta, "Self-focusing dynamics of coupled optical beams," Phys. Rev. A **75**, 023813 (2007).

33. T.T. Xi, X. Lu, and J. Zhang, "Interaction of Light Filaments Generated by Femtosecond Laser Pulses in Air," Phys. Rev. Lett. **96,** 025003 (2006).

34. B. Shim, S.E. Schrauth, C.J. Hensley, L.T Vuong, P. Hui, A.A. Ishaaya, and A.L. Gaeta, "Controlled interactions of femtosecond light filaments in air," Phys. Rev. A **81,** 061803(R) (2010).

# CHAPTER 2

## PULSE SPLITTING IN THE ANOMALOUS GROUP VELOCITY DISPERSION REGIME[1]

With the advent of ultrashort lasers, the study of high intensity light interactions with matter became possible. A high-power laser pulse will experience an intensity-dependent refractive index, which can result in self-focusing if the power $P$ of a laser pulse is greater than a certain critical power $P_{cr}$. Although much of the initial work dealt with spatial effects, the dynamics of spatio-temporal wave collapse has generated significant interest [1-3] and includes a broad range of phenomena including pulse compression, pulse-splitting, supercontinuum generation, harmonic generation, plasma formation, and filamentation [4, 5]. One of the fundamental dynamical effects that arises from the interplay of nonlinearity and normal group-velocity dispersion (GVD) is pulse-splitting [2, 3, 6, 7], which was demonstrated experimentally [8-13]. In the anomalous-GVD regime, temporal dynamics during beam collapse has not been extensively explored [14-16], and it was generally believed that the pulse should exhibit full spatio-temporal collapse.

Recent investigations of the spatial dynamics of a collapsing super-Gaussian beam show a behavior distinct from that for a Gaussian beam. Theory predicts that as the beam self-focuses the transverse profile evolves initially to a ring solution [17, 18], which was confirmed experimentally [19]. These results provided compelling evidence for the role of the initial beam shape on the spatial collapse dynamics, and motivated the development of the nonlinear geometrical optics (NGO) method for analyzing beam collapse without the need for full integration of the 3-D nonlinear Schödinger equation [18]. Two key NGO predictions are that the

[1] S.E. Schrauth, B. Shim, A.D. Slepkov, L.T. Vuong, A.L. Gaeta, N. Gavish, and G. Fibich, "Pulse-splitting in the anomalous group-velocity-dispersion regime," Opt. Express, **19**, 9309-9314 (2011).

initial temporal dynamics in the anomalous-GVD regime is decoupled from the spatial dynamics and that it should depend on the temporal pulse shape in a manner entirely analogous to that exhibited in the spatial regime.

In this work we confirm these predictions experimentally, by propagating ultrashort pulses in the anomalous-GVD regime in a fused-silica sample at powers several times $P_{cr}$. We observe that temporal super-Gaussian input pulses undergo pulse-splitting, whereas Gaussian ones do not. To the best of our knowledge, no previous experimental work has shown that the temporal dynamics depend on whether or not the input pulse is temporally flat-top. We also find that no pulse-splitting occurs at the zero-GVD regime, regardless of the initial pulse shape.

### *2.1 Numerical model and results*

We simulate pulse propagation using the nonlinear Schrödinger equation (NLSE) with dispersion for the slowly-varying envelope $A(\eta, \xi, \tau)$ centered at frequency $\omega$,

$$\frac{\partial A}{\partial \xi} = \frac{i}{4}\left(\frac{\partial^2}{\partial \eta^2} + \frac{\partial^2}{\partial \xi^2}\right)A - i\ \mathrm{sgn}\left(\beta_2\right)\frac{L_{df}}{2L_{ds}}\frac{\partial^2 A}{\partial \tau^2} + i\frac{L_{df}}{L_{nl}}\left|A\right|^2 A \qquad (2.1)$$

where $w_0$ is the spot size, $L_{df}=k\,w_0^2/2$ is the diffraction length, $L_{nl}=(n_2 n_0 \omega |A_0|^2/2\pi)^{-1}$ is the nonlinear length, $|A_0|$ is the magnitude of the input laser field, $\eta=x/w_0$ and $\xi$=y/ $w_0$ are the normalized coordinates, $\zeta=z/L_{df}$ is the normalized propagation length, $\tau_p$ is the temporal pulse width, $L_{ds}=\tau_p^2/|\beta_2|$ is the dispersion length, $\tau=[t-(z/v_g)]/\tau_p$ is the normalized retarded time for the pulse traveling at the group velocity $v_g$. Figure 1 shows simulations of the NLSE. All simulations have a Gaussian spatial profile $\exp(-r^2)$ as the input, while the temporal profile is varied. The value of $L_{df}$ / $L_{ds}$ for all simulations is 0.04. Two cases of the collapse of a Gaussian pulse $\exp(-t^2)$ are shown in the top part of the figure. Figure 2.1(a) is $2P_{cr}$ and Figure 2.1(b) is $3P_{cr}$. Overall the temporal dynamics result in 3-D collapse as predicted by previous work. However, for a

super-Gaussian temporal profile exp(-$t^4$), the pulse undergoes splitting, as shown in Figure 2.1(c) for $2P_{cr}$ and Figure 2.1(d) for $3P_{cr}$. In the spatial domain all input profiles are a Gaussian, and therefore they evolve into a peak-type profile.

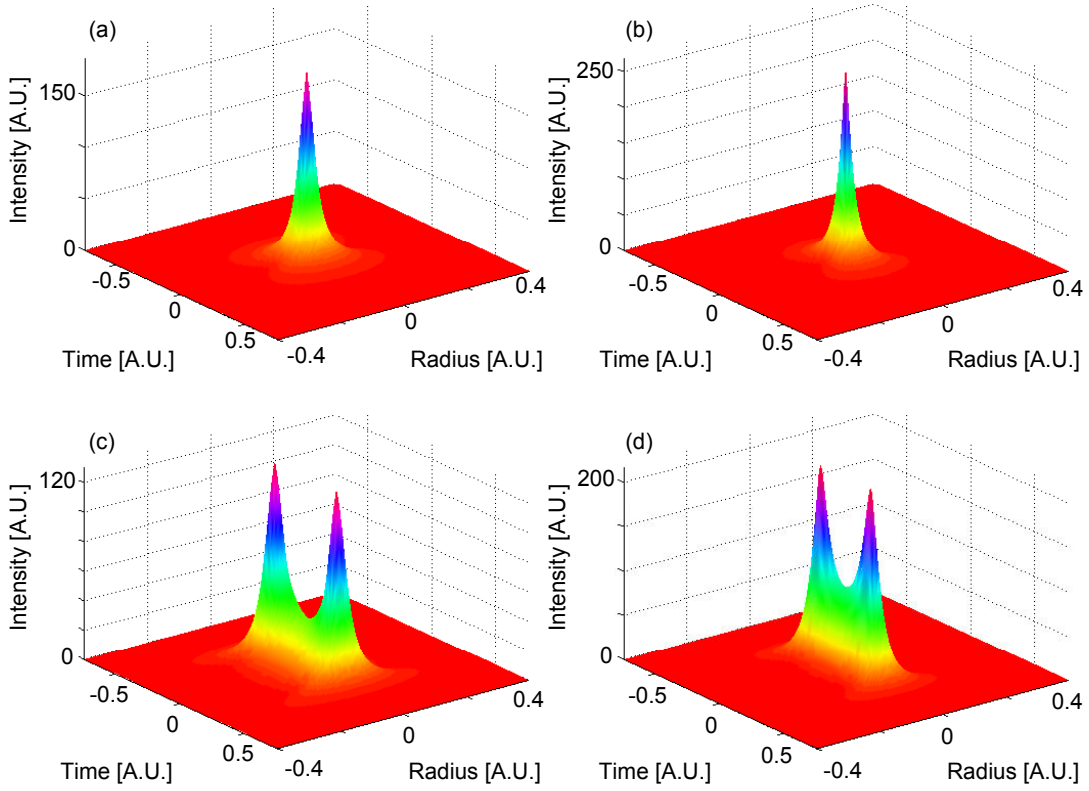


Figure 2.1 Comparison of simulation results for Gaussian temporal profile (top) and super-Gaussian temporal profile (bottom), for input power of $2P_{cr}$ [(a) and (c)], $3P_{cr}$ [(b) and (d)], wavelength of 1550 nm, and $\beta_2$ of -279 fs$^2$/cm. The input spatial profiles for all simulations are Gaussian. The spatio-temporal profiles are taken from the propagation point at which the beam is collapsing and before the intensity becomes sufficiently high that higher order effects change the dynamics.

The pulse dynamics can be explained intuitively by the NGO method [18], which approximates the initial self-focusing dynamics with a reduced system of linear ordinary differential equations. These equations show that initially, the spatial and temporal dynamics are decoupled. The temporal dynamics in the anomalous-GVD regime is governed by the NGO eikonal equation for the ray trajectories,

$$\frac{dT(z)}{dz} = 2z\frac{d}{dT}|\psi_0|^2, \tag{2.2}$$

and by the NGO transport equation for amplitude evolution along the rays,

$$\frac{dC(z)}{dz} = -C\left[T(z)\right] z \frac{d^2}{dT^2}|\psi_0(T)|^2 \tag{2.3}$$

where $T$ is the temporal coordinate of the ray at the propagation distance $z$, $\psi_0$ is the input field and $C$ is the $z$-dependent amplitude. Equations (2) and (3) show that for a high-power temporal profile of the form $\exp(-t^{2m})$, the pulse will undergo splitting if $m > 1$, but will focus to a single peak if $m = 1$ [18], as is confirmed in direct numerical simulations of the NLSE, see Figure 2.1. Comparison of the on-axis temporal profile for $m = 2$ (temporal super-Gaussian), shows a remarkable agreement between the solutions of the NLSE and of the NGO equations, see Figure 2.2. Note that the peaks of the split pulses are at the same temporal position $\tau = \pm 0.2$.

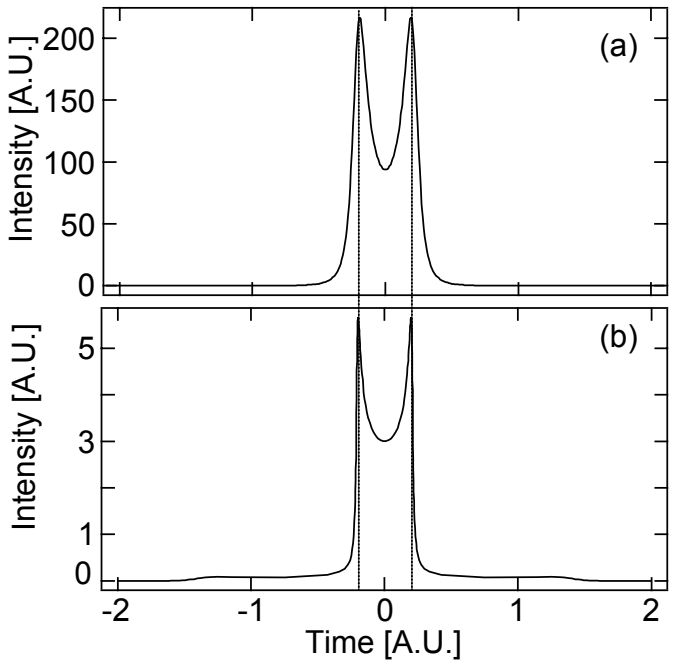


Figure 2.2 Comparison of simulation results for a super-Gaussian temporal profile. The top (a) is the on-axis temporal profile found by directly integrating the NLSE in the anomalous (a) with input power 3, wavelength of 1550 nm, and $\beta_2$ of -279 fs$^2$/cm. The bottom (b) is found using the 1-D building block of the NGO method. Although the profiles are slightly different, the peaks of the split pulses occur at ±0.2 for both direct integration and the NGO method.

### *2.2 Experimental results*

We performed experiments to investigate these predictions with an amplified Ti:sapphire laser system operating at 800 nm, which generates 1.6-mJ, 70-fs pulses at a 1-kHz repetition rate. The output of the amplified system pumps an optical parametric amplifier to produce 150-$\mu$J pulses at 1510 nm or 125-$\mu$J pulses at 1275 nm. These two wavelengths are chosen since they correspond to the anomalous-GVD and the zero-GVD regimes, respectively, for the fused-silica sample. We spatially filter the output and temporally shape the pulse using a standard 4-*f* pulse shaper [20] with a 1-D double-mask liquid-crystal spatial light modulator to tailor the amplitude and phase of the spectrum. The output of the pulse shaper has pulse durations of 200-fs and 160-fs at 1510 nm and 1275 nm, respectively. We focus the outputs of the pulse shaper onto the front face of the sample, with spot sizes of 245 $\mu$m and 185 $\mu$m for 1510 nm and for 1275 nm, respectively. We use a 30-mm fused-silica sample, for which the physical parameters are as follows: at 1510 nm $\beta_2$ = -279 fs$^2$/cm and $n_2$ = 2.2x10$^{-16}$ cm$^2$/W, and at 1275 nm $\beta_2$ = 1 fs$^2$/cm and $n_2$ = 2.5 x10$^{-16}$ cm$^2$/W [15]. Upon propagation through the sample, we use a two-photon autocorrelator [21] and an optical spectrum analyzer as diagnostics.

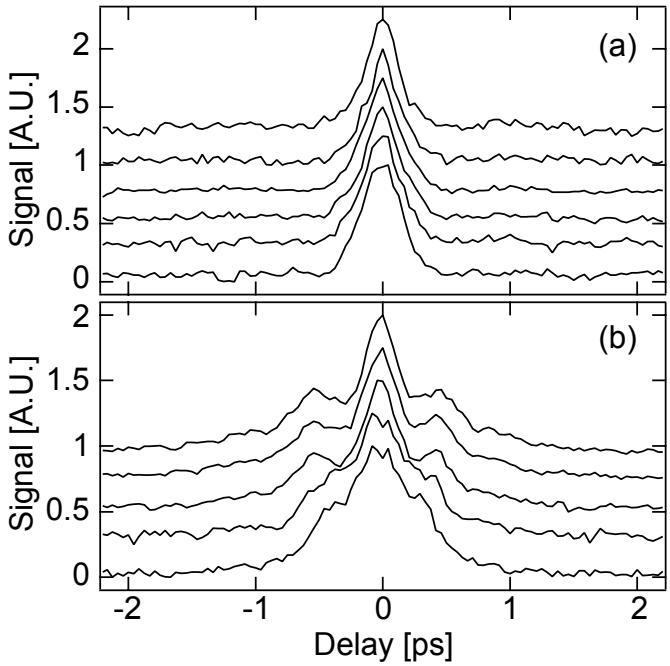


Figure 2.3 Autocorrelation traces after propagation through 30 mm of fused silica at a wavelength of 1510 nm. The top plot (a) is for a temporal Gaussian input profile with peak power increasing from bottom to top ($P$ = 15.7 MW, 24.7 MW, 33.7 MW, 41.5 MW, 49.4 MW, 62.8 MW). The lower plot (b) is for a temporal super-Gaussian input profile with peak power increasing from bottom to top ($P$ = 11.2 MW, 14.6 MW, 18.0 MW, 21.8 MW, 26.9 MW). For the super-Gaussian case the pulse-splitting is pronounced as the power is increased.

The autocorrelation of the pulse for various powers after propagation through the 30-mm fused-silica sample is shown in Figure 2.3. The traces in Figure 2.3(a) are the autocorrelations for a temporal Gaussian input profile through the sample. The energy increases from the bottom to the top trace. As the energy is increased, there is no indication of any pulse-splitting. The traces in Figure 2.3(b) are the autocorrelations for a temporal super-Gaussian input through the sample. They exhibit pulse splitting at the lowest peak power as evidenced by the appearance of shoulders on the autocorrelation trace, and as the energy is increased the pulse-splitting becomes more pronounced. These observations are consistent with our theoretical predictions.

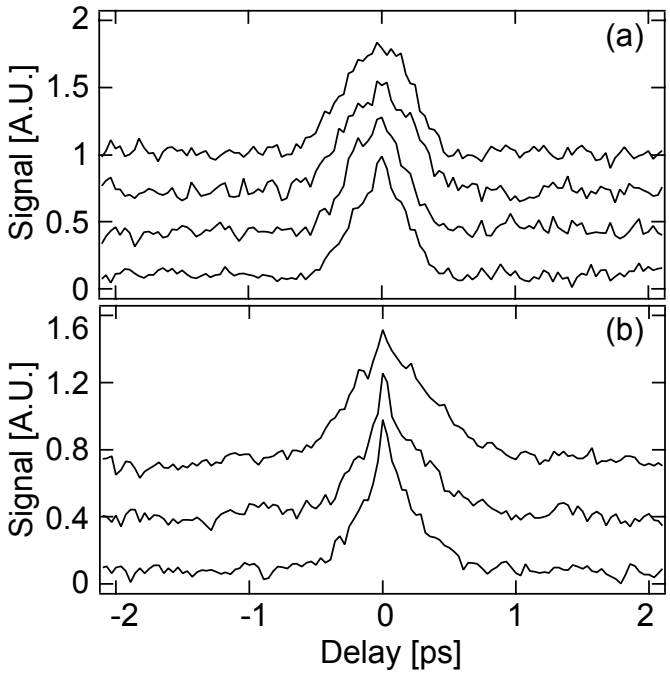


Figure 2.4 Pulse autocorrelation traces after propagation through 30-mm of fused-silica at wavelength of 1275 nm. The top plot (a) is for a temporal Gaussian input profile with power increasing from bottom to top ($P$ = 33.8 MW, 50.7 MW, 67.6 MW, 84.5 MW). The lower plot (b) is for a temporal super-Gaussian input profile with power increasing from bottom to top ($P$ = 19.7 MW, 29.6 MW, 45.1 MW). Pulse-splitting does not occur in either case.

As a comparison, we also perform the analogous experiment with pulses at 1275 nm, at which point the GVD is nearly zero (i.e., $\beta_2 = 1$ fs$^2$/cm). As expected, we do not observe pulse-splitting at this wavelength for either a Gaussian pulse [Figure 2.4(a)] or for a super-Gaussian pulse [Figure 2.4(b)] for the range of powers studied, which indicates that the pulse-splitting of super-Gaussian pulses should only occur in the anomalous-GVD regime, as predicted.

### *2.3 Conclusions*

In conclusion, we show that the spatio-temporal dynamics strongly depends on the temporal profile of the pulse. We observe that pulse-splitting can occur in the anomalous-GVD regime for the case of super-Gaussian input pulses, which confirms recent theoretical predictions. This splitting can be interpreted as a temporal focusing of the energy in the beam due to strong self-

phase modulation, and is analogous to the spatial focusing of the beam to a ring profile for a super-Gaussian spatial profile [17-19]. These results are relevant to understanding how shaping the temporal profile of the initial pulse can dramatically change the temporal dynamics and the filamentation and plasma formation process. Finally, we note that this splitting is very different from the one in the normal-GVD regime. Indeed, in the normal GVD regime, both Gaussian and super-Gaussian pulses undergo a temporal splitting. Moreover, this temporal splitting strongly depends on the spatial dynamics, since it only occurs after the pulse undergoes a significant spatial self-focusing, and it is associated with a departure from a self-similar Townes spatial profile [7].

REFERENCES


1. R.Y. Chiao, E. Garmire, and C.H. Townes, "Self-trapping of optical beams" Phys. Rev. Lett. **13**, 479-482 (1964).

2. N.A. Zharova, A.G. Litvak, T.A. Petrova, A.M. Sergeev, and A.D Yunakovskii, "Multiple fractionation of wave structure in a nonlinear medium," Pis'ma Zh. Eksp. Teor. Fiz. **44**, 13-17 (1986).

3. S.N. Vlasov, L.V. Piskunova, and V.I. Talanov, "Three-dimensional wave collapse in the nonlinear Schrödinger equation model," Zh. Eksp. Teor. Fiz. **95**, 1945-1950 (1989).

4. A.L. Gaeta, "Catastrophic collapse of ultrashort pulses," Phys. Rev. Lett. **84**, 3582-3585 (2000).

5. A. Couairon and A. Mysyrowicz, "Femtosecond filamentation in transparent media," Phys. Rep., **441**, 47-189 (2007).

6. J.E. Rothenberg, "Pulse splitting during self-focusing in normally dispersive media," Opt. Lett. **17**, 583-585 (1992).

7. G. Fibich, V.M. Malkin, and G.C. Papanicolaou, "Beam self-focusing in the presence of a small normal time dispersion," Phys. Rev. A **52**, 4218-4228 (1995).

8. J.K. Ranka, R.W. Schirmer, and A.L. Gaeta, "Observation of pulse splitting in nonlinear dispersive media," Phys. Rev. Lett. **77**, 3783-3786 (1996).

9. S.A. Diddams, H.K. Eaton, A.A. Zozulya, and T.S. Clement, "Amplitude and phase measurements of femtosecond pulse splitting in nonlinear dispersive media," Opt. Lett. **23**, 379-381 (1998).

10. A.A. Zozulya, S.A. Diddams, A.G. Van Engen, and T.S. Clement, "Propagation dynamics of intense femtosecond pulses: multiple splittings, coalescence, and continuum generation," Phys. Rev. Lett. **82**, 1430-1433 (1999).

11. A.A. Zozulya, S.A. Diddams, and T.S. Clement, "Investigations of nonlinear femtosecond pulse propagation with the inclusion of Raman, shock, and third-order phase effects," Phys. Rev. A **58**, 3303-3310 (1998).

12. S. Tzortzakis, L. Sudrie, M. Franco, B. Prade, A. Mysyrowicz, A. Couairon, and L. Bergé, "Self-guided propagation of ultrashort IR laser pulses in fused silica," Phys. Rev. Lett. **87**, 213902 (2001).

13. K.D. Moll and A.L. Gaeta, "Role of dispersion in multiple-collapse dynamics," Opt. Lett. **29**, 995-997 (2004).

14. M. Trippenbach and Y.B. Band, "Effects of self-steepening and self-frequency shifting on short-pulse splitting in dispersive nonlinear media," Phys. Rev. A **57**, 4791-4803 (1998).

15. S. Skupin and L. Bergé, "Self-guiding of femtosecond light pulses in condensed media: Plasma generation versus chromatic dispersion," Physica D **220**, 14-30 (2006).

16. J. Liu, R. Li, and Z. Xu, "Few-cycle spatiotemporal soliton wave excited by filamentation of a femtosecond laser pulse in materials with anomalous dispersion," Phys. Rev. A **74**, 043801 (2006).

17. G. Fibich, N. Gavish, and X. Wang, "Singular ring solutions of critical and supercritical nonlinear Schrödinger equations," Physica D **231**, 55-86 (2007).

18. N. Gavish, G. Fibich, L.T. Vuong, and A.L. Gaeta, "Predicting the filamentation of high-power beams and pulses without numerical integration: A nonlinear geometrical optics method," Phys. Rev. A **78**, 043807 (2008).

19. T.D. Grow, A.A. Ishaaya, L.T. Vuong, A.L. Gaeta, N. Gavish, and G. Fibich, "Collapse dynamics of super-Gaussian beams," Opt. Exp. **14**, 5468-5475 (2006).

20. A.M. Weiner, J.P. Heritage, and E.M. Kirschner, "High-resolution femtosecond pulse shaping," J. Opt. Soc. Am. B **5**, 1563-1572 (1998).

21. J.K. Ranka, A.L. Gaeta, A. Baltuska, M.S. Pshenichnikov, and D.A. Wiersma, "Autocorrelation measurement of 6-fs pulses based on the two-photon-induced photocurrent in a GaAsP photodiode," Opt. Lett. **22**, 1344-1346 (1997).

# CHAPTER 3

## SELF-FOCUSING OF HIGHER-ORDER MODES IN OPTICAL FIBERS

Recent advances in fabrication techniques for optical fiber has resulted in much higher quality fiber. The quality has improved such that one of the limitations on the power that can be propagated through a fiber is the nonlinear refractive index of the fiber. The maximum power able to be transmitted through optical fibers is approaching the critical power for self-focusing of a radially symmetric beam, $P_{CR}$ [1-6]. The design of high-power fiber lasers and fiber amplifiers is one of the main areas of interest for the guidance of high power pulses. In addition to propagation in step-index fibers, there has been interest in guiding high power pulses through gas filled capillaries for things such as high-harmonic generation [7].

This has resulted in a large amount of effort and interest in the nonlinear propagation of high-power pulses in waveguides. One area of research has been looking at the propagation in simple, multimode step-index fibers. There has been work looking at the propagation of $LP_{\nu 1}$, but for $\nu$'s only up to 3 [8]. They found an increase in self-focusing distance with increasing values of $\nu$. There have been other studies looking at the propagation of the fundamental mode of a multimode fiber, with the main interest being the nonlinear broadening in such fibers [9]. Other work on ultra-large-mode-area fibers studied the self-focusing length of a summation of many input modes [10].

At the same time, there has been an effort to design and develop and produce specialty fiber designs and technologies that allow for the generation and guidance of few MW pulses. For wavelengths from near infrared to the common infrared communications wavelengths, this power is on the order of a few MW. Specifically, the critical power $P_{CR}$ is 2 MW at 800 nm and

11 MW at 1550 nm. Many schemes have been devised to allow the guidance of such high powers while mitigating the effects of beam collapse. One example is fabricating fibers with a low index defect in the center of the fiber [11]. This does not allow for guiding of the fundamental Townes profile, which is the ground state solution to the bulk Nonlinear Schrödinger Equation (NLSE) [1, 3]. The propagation then takes place in a higher-order radially symmetric mode, such as $LP_{02}$. Another fiber design, utilizing long period gratings, converts a fundamental input mode into a single radially symmetric higher-order mode of a large mode area fiber. The field then propagates in this single radially symmetric higher order mode [12, 13]. There has also been work looking at the propagation of high-power beams in high-aspect ratio rectangular core fibers [14, 15]. These designs are good, but we want to study the propagation of the higher-order modes of step-index fibers, without having a specially designed fiber, which can be difficult to produce.

In addition to interest in waveguides, there has been work done on beams that propagate in bulk with a power higher than the critical power for collapse for a radially symmetric beam. Work has been done on the collapse threshold of elliptical beams, finding a small increase in the collapse threshold for increasing ellipticity [15, 16]. In addition to work on elliptically shaped beam, there has also been work on the bulk propagation of necklace beams in Kerr media [16-19]. For radially symmetric beams, the power of collapse is a few percent higher than the power of the Townes profile, $P_{CR}$, in both bulk and waveguides [3]. This small difference is due to a shape dependent factor. There have been theoretical predictions that in Kerr media, necklace beams are stable upon bulk propagation [18-21]. It has also been shown experimentally that necklace like beams resist collapse up to a certain power threshold. The critical power for collapse of necklace like beams is approximately the number of bead multiplied by $P_{CR}$, the

critical power for collapse of a radially symmetric beam [21]. The simple explanation of this stabilization has to do with the interaction between adjacent beads. The interaction depends on the size of the beads and the separation between them [20]. When each bead has less than a critical power, each individual bead cannot collapse and the beam size will remain relatively large and there will be repulsive interactions between a bead and its two neighbors. As this is occurring, the beam will also be diffracting, so that the intensity falls with propagation distance and the self-focusing gets weaker. When there is more than a critical power for each bead, each bead starts to collapse. As it collapses, the size of each bead gets smaller and the intensity dependent refractive index result in more self-focusing for each bead. Once the bead is below a certain size, it no longer interacts and hence, no longer can be stabilized by its out-of-phase, neighboring beads. So, there has been a large amount of interest in how the different initial beam shapes can effect the nonlinear propagation, such as critical power or collapse distance.

The interest in beams with higher collapse thresholds leads naturally to studying these specific beam profiles in fibers. The rectangular core fibers that have been designed and developed were intended to take advantage of the higher collapse threshold of rectangular beams [14], or the multi-moded, for higher-order modes, nature of the high-aspect ratio, rectangular core fibers. Due to this increase in collapse threshold of necklace like beams, we are interested in whether these beams allow for high-power propagation in a waveguide. In addition to the increase in collapse threshold, the beam shape of necklace beams is an advantage for propagation in fibers. It turns out that for standard step-index fibers, using the weakly guiding approximation, the $LP_{\nu 1}$ modes are very much like the necklace or Laguerre-Gaussian beams studied theoretically and experimentally. There are $2\nu$ beads and each bead is $\pi$ out-of-phase with the adjacent beads. The other advantage is that there has been experimental work on the

generation of necklace like beams in bulk and in waveguides. The generation of these necklace type beams has been achieved with long-period gratings [12, 13], an optical phase shifter [21], a phase mask [22], and fiber structures [23]. The bulk self-focusing advantage, interest in high-power throughput through fiber, and the prevalence of methods for generation of necklace type beams all point towards the importance of studying the propagation at high-power in fibers.

### *3.1 Numerical model*

To investigate this, we perform simulations modeling the propagation using the standard split step method to numerically integrate the normalized nonlinear Schrödinger equation (NLSE),

$$\frac{\partial}{\partial\zeta}\psi = \frac{i}{4}\left(\frac{\partial^2}{\partial\eta^2}+\frac{\partial^2}{\partial\xi^2}\right)\psi + i\frac{L_{DF}}{L_{NL}}|\psi|^2\psi + \mathrm{f}(\eta,\xi)\psi\,, \qquad (3.1)$$

where $\psi(\eta,\xi,\zeta)=A(x,y,z)/A_0$ is the normalized field, $L_{DF}=\pi n_0 w_0^2/\lambda$ is the diffraction length, $n_0$ is the refractive index of the core, $w_0$ is the characteristic radius, $\lambda$ is the wavelength, $\eta = x/w_0$ is the normalized x coordinate, $\xi = y/w_0$ is the normalized y coordinate, $\zeta = z/L_{DF}$ is the normalized z coordinate, $L_{NL} = (n_2 n_0 \omega|A_0|^2/2\pi)^{-1}$ is the nonlinear length, $\omega$ is the angular frequency of the light, $n_2$ is the intensity dependent refractive index, and $|A_0|$ is the magnitude of the field. It should be noted that $w_0$ is the radius of the peak of the field at the input, which is similar to the convention used by Grow *et. al* [21]. The first term on the right is the diffraction term. The second term gives rise to the intensity-dependent refractive index. The final term, f($\eta$, $\xi$) takes into account the index profile of the waveguide [26] or for the hollow metallic waveguide, the absorptive boundary condition. For the dielectric waveguide it accounts for the phase difference between the part of the field propagating in the core to the part of the field propagating in the cladding. For the case of a circular step-index waveguide, which we are interested in here, the f is,

$$\mathrm{f} = \begin{cases} -i\dfrac{\Delta n_0 \omega}{c} L_{DF}\left(1 - \dfrac{\Delta n}{2}\right), r > r_0 \\ 0, r < r_0 \end{cases}, \qquad (3.2)$$

where $\Delta n$ is the index difference between the core and the cladding, $r_0$ is the radius of the core, and $c$ is the speed of light. We do not model the propagation through with bends in the fiber. The fiber is assumed to be straight. We confirmed our model for the propagation of low power modes of the waveguides. The results of these simulations showed the expected guidance of the low-power fundamental mode and of low-power $LP_{v1}$ modes. Using this model based on the NLSE, we can start exploring the high-power propagation of $LP_{v1}$ modes in step-index fiber.

To model the propagation, we use the split-step Fourier method [27]. This method consists of alternating between the linear spatial propagation and the nonlinear (self-focusing) propagation. The linear propagation is treated by performing a Fourier transform on equation 3.1, while neglecting the nonlinear and waveguide part. Once in Fourier space, the propagation is account for by multiplication by a quadratic phase factor, over one half step, $h$. This result is then inversely transformed back into real space. To take into account the nonlinear and waveguide terms, we neglect the diffraction term and take a full step, $2h$. When the diffraction term is neglected then equation 3.1 can just be integrated over the $2h$ step, noting that the partial derivative in $\zeta$ of $|\psi|^2$ is easily shown to be a constant. In this approximation, the nonlinear term and the waveguide term result in a spatially dependent phase factor. Finally, we repeat the diffraction step over the final half step $h$. For all of the simulations, the step-size $h$ was 0.0005 $L_{DF}$ and the normalized simulation window had transverse dimensions of 2.5 $w_0$ by 2.5 $w_0$ and the grid size was 4096x4096.

### *3.2 Dielectric waveguide results*

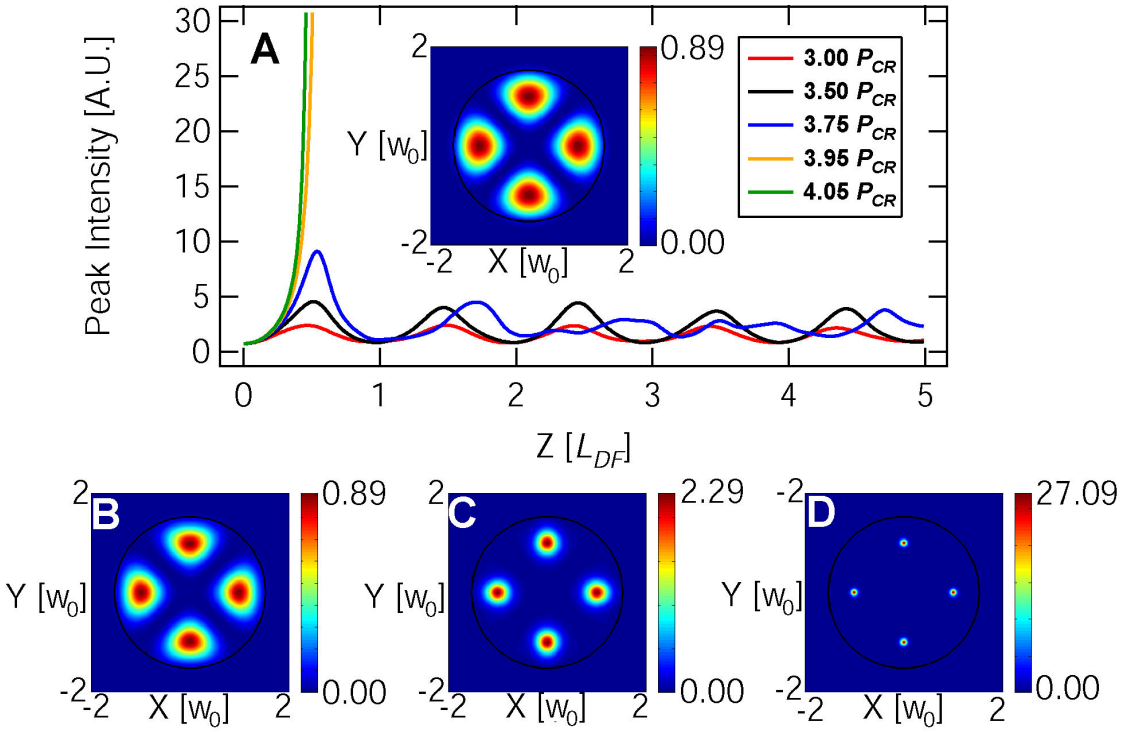


Figure 3.1. A. The normalized peak intensity for an input $LP_{21}$ for the waveguide with a radius of 14.0 micron, with input powers 3.00, 3.50, 3.75, 3.95, and 4.05 $P_{CR}$. The inset is the input mode with the solid black line denoting the core-cladding interface. B. Output profile for 3.00 $P_{CR}$ C. Output profile for 3.75 $P_{CR}$. D. Profile for 3.95 $P_{CR}$ at 0.50 $L_{DF}$.

For our simulations we model two step-index waveguides with different radii, but a Δn of 0.0033. We first test a fiber with a smaller radius, 14.0 microns. The parameters are similar to those of a commercially available step-index fiber with V# = 10.7627. This multi-mode fiber supports the $LP_{\nu 1}$ up to ν = 7 at 800 nm. The peak intensity for the propagation of $LP_{21}$ and output beam profiles is shown in Figure 3.1. For the $LP_{21}$ input with powers up to 3.75 $P_{CR}$ we see stable propagation, with some oscillation in the peak intensity of the beads. For 3.95 $P_{CR}$, an increase of only 0.05 $P_{CR}$ per bead, we see that the beam profile very quickly collapses. This mode profile can be thought of as an approximation of a necklace beam with 4 beads. Based on the results of Grow *et. al*, the critical power for collapse in the bulk is estimated as ~4 $P_{CR}$. The peak intensity for an input of 4.00 $P_{CR}$ is shown as this limiting case. We see that for the $LP_{21}$ there is an improvement in the collapse threshold over the case of the radially symmetric

fundamental mode, which collapses at 1 $P_{CR}$ [3, 5]. Using the same waveguides parameters, we simulate the propagation of the $LP_{31}$ mode, the results are shown in Figure 3.2. Again, we see similar dynamics, where input powers of 4.00 $P_{CR}$ and 5.00 $P_{CR}$ propagate with some oscillation. Here, we see that there is collapse over these distances for an input power of 5.25 $P_{CR}$.

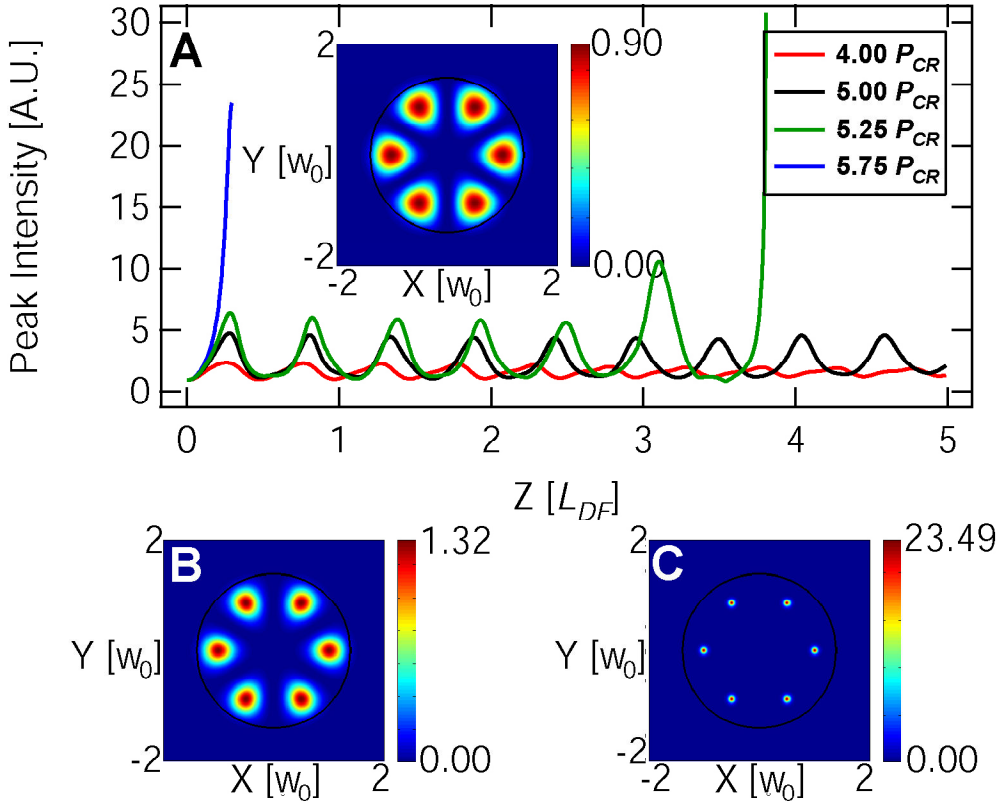


Figure 3.2 A. The normalized peak intensity for an input $LP_{31}$ for the waveguide with the a radius of 14.0 micron, with input powers 4.00, 5.00, 5.25, 5.75 $P_{CR}$. The inset is the input mode with the solid black line denoting the core-cladding interface. B. Output profile for 4.00 $P_{CR}$ C. Output profile for 5.75 $P_{CR}$ at 0.296 $L_{DF}$.

As a further test of the propagation dynamics in fibers, we simulate the propagation in a larger core fiber, 50 microns, with the rest of the fiber parameters remaining the same. This is similar in size to the fibers that have been developed for use in fiber lasers and fiber amplifiers by other groups [10, 12, 13]. The other interesting aspect when compared with the smaller core is that the larger core fiber can guide many more modes. This gives us an idea how much of an affect the fiber size has on the high-power propagation dynamics. The simulations for the $LP_{21}$ mode and the $LP_{31}$ mode are shown in Figure 3.3 and Figure 3.4, respectively. We see very similar propagation dynamics for the smaller (14 micron) core fiber and the larger (50 micron)

core fiber. The main difference is that there are more oscillations in the peak intensity for the larger core fiber. This is simply due to there being more guided modes for the larger fiber so as the beam propagates and self-focuses, other higher-order modes are excited. It does not appear to affect the high-power propagation dynamics. This leads us to believe in that in these types of fibers, any benefit to collapse threshold or collapse distance is due to the shape of the beam, not any inherent property of the fiber. For example, the collapse of the $LP_{21}$ with 3.95 $P_{CR}$ occurs at 0.5 $L_{DF}$ in the smaller core fiber and occurs at 0.58 $L_{DF}$ in the larger core fiber.

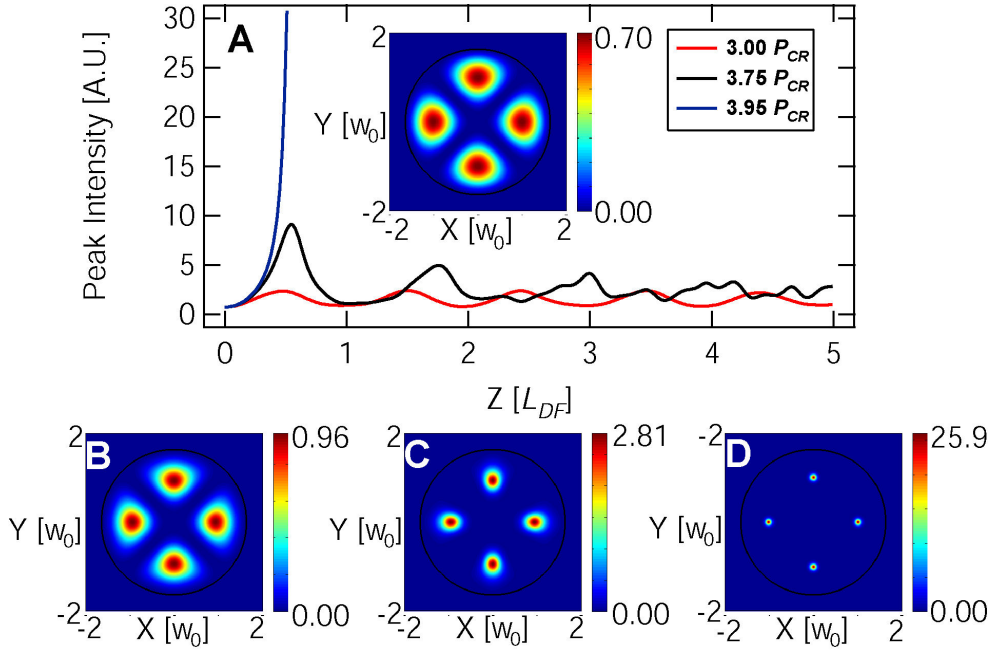


Figure 3.3 A. The normalized peak intensity for an input $LP_{21}$ for the waveguide with a radius of 50.0 micron, with input powers 3.00, 3.75, and 3.95 $P_{CR}$. The inset is the input mode with the solid black line denoting the core-cladding interface. B. Output profile for 3.00 $P_{CR}$ C. Output profile for 3.75 $P_{CR}$ D. Profile for 3.95 $P_{CR}$ at 0.58 $L_{DF}$.

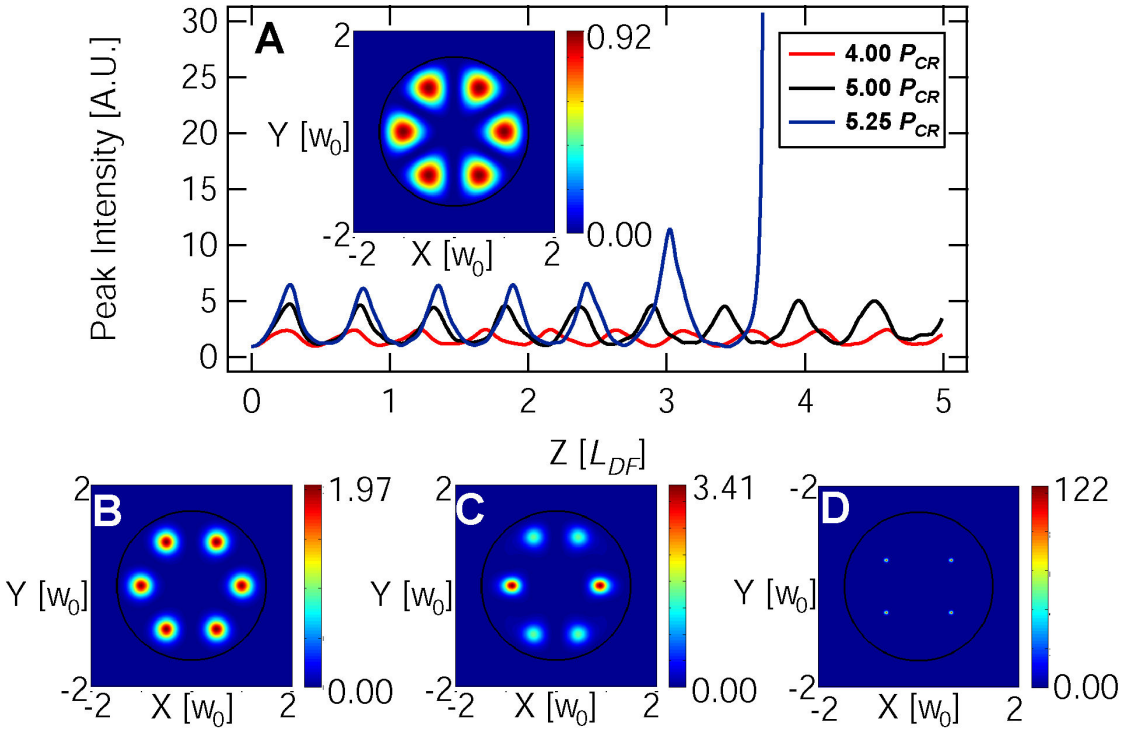


Figure 3.4 A. The normalized peak intensity for an input $LP_{31}$ for the waveguide with a radius of 50.0 micron, with input powers 4.00, 5.00, and 5.25 $P_{CR}$. The inset is the input mode with the solid black line denoting the core-cladding interface. B. Output profile for 4.00 $P_{CR}$ C. Output profile for 5.00 $P_{CR}$ D. Profile for 5.25 $P_{CR}$ at 3.725 $L_{DF}$.

With these simulations looking specifically at the propagation of the necklace type beams, we can say that there is a benefit in terms of collapse threshold and distance for the distances studied. The collapse threshold is shown in Figure 3.5. The line denotes the bulk threshold as determined experimentally [21]. The red squares are the numerically determined collapse threshold from our simulations. We believe this saturation is due to the confinement of the beam provided by the fiber. This is different from the bulk case, because in bulk the necklace beams either collapse or diffract and the intensity decrease monotonically. For the propagation in fibers, the energy remains in the fiber; this is evidenced by the oscillations shown in the peak intensity in Figures 3.1-3.4.

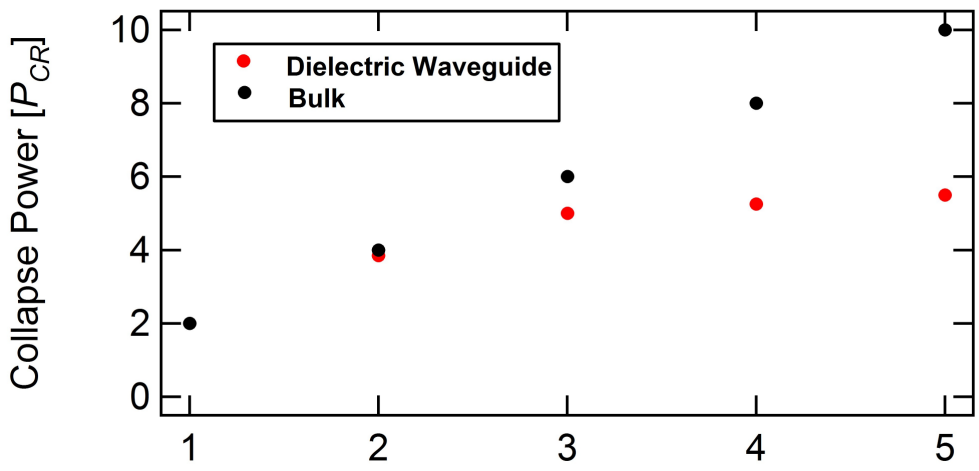


Figure 3.5. The collapse threshold for unperturbed beams over these distances studied in the simulations. For the lower values of ν the collapse threshold follows that of the bulk case. As ν is increased, the collapse threshold appears to saturate.

So far, the simulations have been done with inputs that are exactly an $LP_{\nu 1}$ mode. To see the affect a perturbation would have on the propagation dynamics, we looked at what would happen if one of the beads had an amplitude that is 1.01 times larger than the other beads. This corresponds to the perturbed bead having 1.02 times the power contained in each of the other beads. We looked at the $LP_{31}$ mode in the waveguide with the 50 micron radius. The results of the simulations are shown in Figure 3.6. When the input beam has this perturbation we see collapse at much shorter distances then the case where the input is an unperturbed $LP_{\nu 1}$ mode of the fiber. This is due to the fact that the slight perturbation on one bead of the input means the input is no longer a single pure $LP_{\nu 1}$ mode of the fiber. There is one predominant ν, but there are others that are propagating as well. In the linear case the different modes would propagate and the profile would evolve based on the propagation constants of the specific modes, resulting in interference between modes, but no interactions. For the nonlinear propagation, the modes will still interact, like the linear case, but there would also be interactions between the modes due to the nonlinearity. Along the propagation, it appears the power in each bead changes. This is in stark contrast to the unperturbed nonlinear propagation. The peak intensities for propagation of perturbed and unperturbed beams are shown in Figures 3.6-3.9 for the $LP_{11}$- $LP_{41}$ modes with

unperturbed and perturbed beam profiles. The power is over the entire beam. For the unperturbed $LP_{11}$- $LP_{41}$ modes, the unperturbed case propagates for at least 15 $L_{DF}$ with all the beads having equal power. The beam profiles at the end of the propagation are shown. Note that the beads all have the same intensity and thus contain the same power at the end of propagation. With the overall same power, but a slightly perturbed mode, then the beam collapses. The beam evolves with power switching between beads. Eventually, part of the profile will contain power greater than one critical power. At this point, that beam will collapse. The profiles during collapse are shown. The propagation distances at which the beam collapses are 8.90 $L_{DF}$, 14.125 $L_{DF}$, 11.95 $L_{DF}$, and 14.75 $L_{DF}$ for the perturbed $LP_{11}$, $LP_{21}$, $LP_{31}$, and $LP_{41}$ respectively.

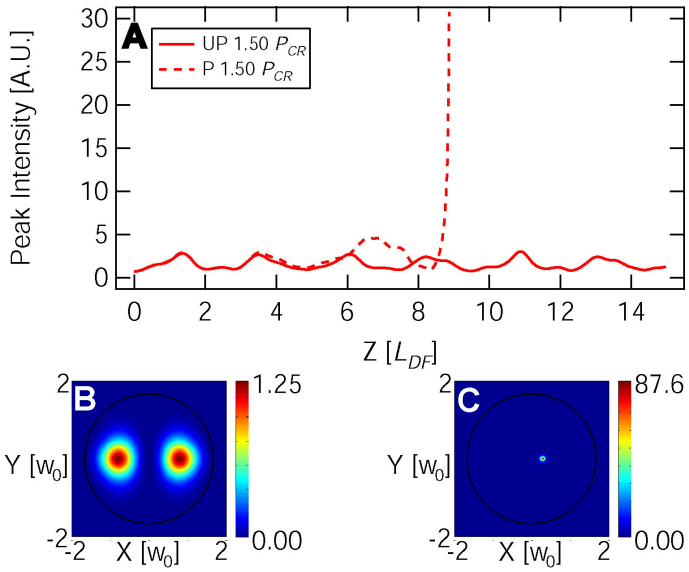


Figure 3.6. A. Peak intensity versus distance for the unperturbed (UP) beam and perturbed (P) beam for the $LP_{11}$ mode of the 50 micron radius fiber. B. The beam profile after 15 $L_{DF}$ propagation for the unperturbed input. C. The beam profile as the beam is collapsing for the perturbed inputs of $LP_{11}$. The distance at which the profile is taken is 8.90 $L_{DF}$.

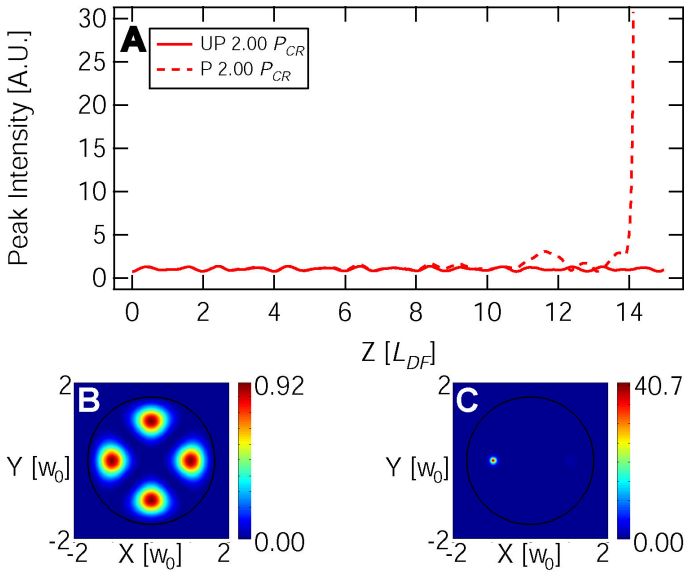


Figure 3.7. A. Peak intensity versus distance for the unperturbed (UP) beam and perturbed (P) beam for the $LP_{21}$ mode of the 50 micron radius fiber. B. The beam profile after 15 $L_{DF}$ propagation for the unperturbed input. C. The beam profile as the beam is collapsing for the perturbed inputs of $LP_{21}$. The distance at which the profile is taken is 14.125 $L_{DF}$.

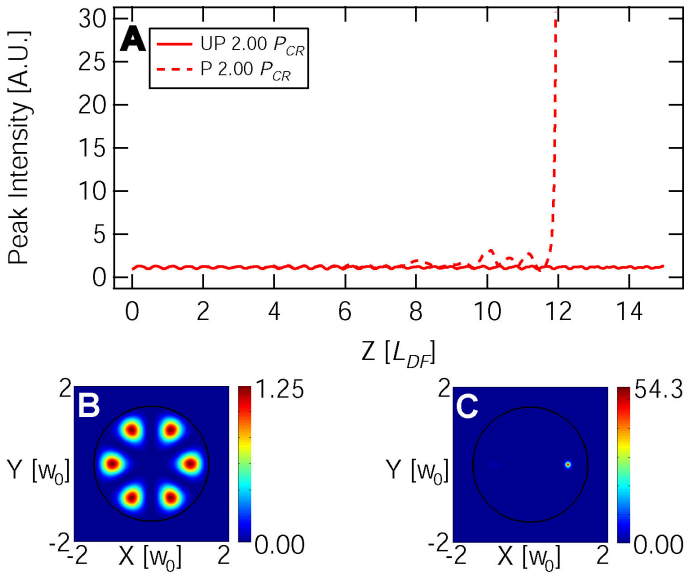


Figure 3.8. A. Peak intensity versus distance for the unperturbed (UP) beam and perturbed (P) beam for the $LP_{31}$ mode of the 50 micron radius fiber. B. The beam profile after 15 $L_{DF}$ propagation for the unperturbed input. C. The beam profile as the beam is collapsing for the perturbed inputs of $LP_{31}$. The distance at which the profile is taken is 11.95 $L_{DF}$.

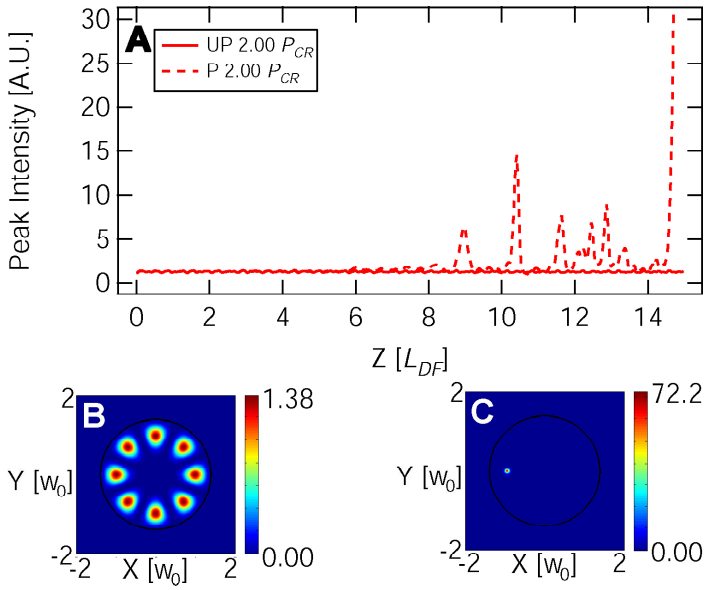


Figure 3.9. A. Peak intensity versus distance for the unperturbed (UP) beam and perturbed (P) beam for the $LP_{41}$ mode of the 50 micron radius fiber. B. The beam profile after 15 $L_{DF}$ propagation for the unperturbed input. C. The beam profile as the beam is collapsing for the perturbed inputs of $LP_{41}$. The distance at which the profile is taken is 14.75 $L_{DF}$.

Finally we can look at how the propagation of the perturbed modes with different powers compares to the propagation of an unperturbed mode with a set power. The simulation results are shown in Figure 3.10. We see that for the unperturbed case of an input $LP_{31}$ with 2.00 $P_{CR}$, the beam propagates over the entire distance. The final beam profile can be seen in 3.10 B. For the case of a perturbed $LP_{31}$ input, the beam collapses as it propagates. The beam profiles for the perturbed input with powers 1.25 $P_{CR}$, 1.50 $P_{CR}$, and 2.00 $P_{CR}$ are shown in Figure 3.10 C-E. The beams propagate 17.5 $L_{DF}$, 15.75 $L_{DF}$, and 11.95 $L_{DF}$ respectively.

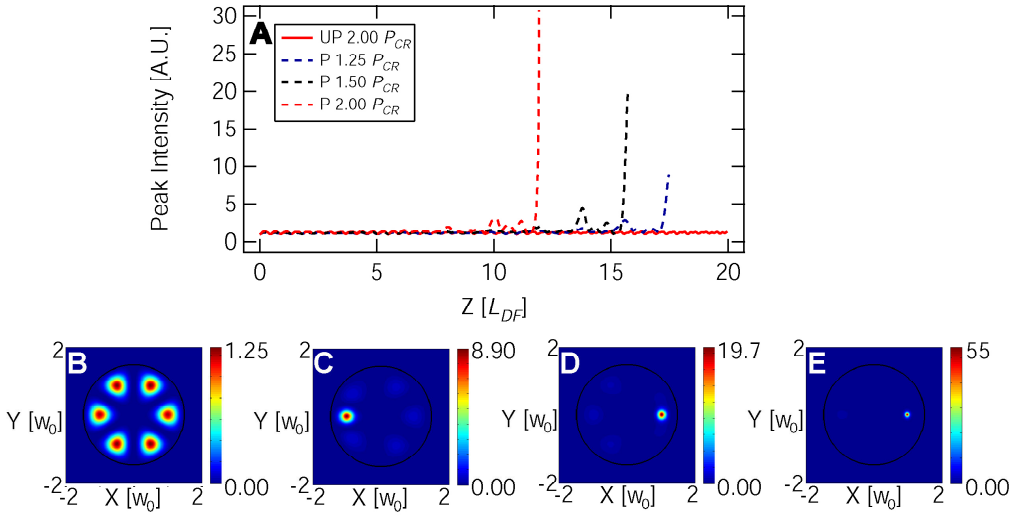


Figure 3.10 A. Comparison of the peak intensity of the unperturbed (UP) LP31 mode with the perturbed (P) $LP_{31}$ mode. B. Beam profile for unperturbed case with input power of 2.00 $P_{CR}$ at 20.0 $L_{DF}$. C. Beam profile for perturbed case with input power of 1.25 $P_{CR}$ at 17.5 $L_{DF}$. D. Beam profile for perturbed case with input power of 1.50 $P_{CR}$ at 15.75 $L_{DF}$. E. Beam profile for perturbed case with input power of 2.00 $P_{CR}$ at 11.95 $L_{DF}$.

The propagation of high-power, higher-order $LP_{v1}$ modes in fibers is found to be possible numerically. The power able to be transmitted over the distances studied does increase, though not to the threshold that is predicted for the collapse of necklace beams in bulk media. In addition, we observe the importance of the exciting the particular mode in attaining this benefit.

### *3.3 Hollow waveguide results*

Also of interest is the case of a hollow waveguide. This is due to recent experimental results with high pressure gases in hollow capillaries where the input power is near or above the critical power [7]. In order to model this, we can use the same model we used for the step index waveguide, but with a f=0 in equation 1.1 and an absorbing boundary to model the metallic walls,

$$\psi = \begin{cases} \psi & r < r_0 \\ 0 & r > r_0 \end{cases} \tag{3.3}$$

where $r_0$ is the radius of the hollow waveguide. For our simulations we set this radius to 200 microns, which is similar to the inner diameter of many hollow glass capillaries used in gas-filled capillary experiments. The peak intensity as a function of propagation distance is shown in Figures 3.11-3.14 for the $LP_{11}$-$LP_{41}$ modes. The collapse threshold is shown in Figure 3.15. The collapse threshold is stated in the number of critical powers. The expectation for the bulk case is also shown as the line. We see that initially the collapse power follows the expectation for bulk, much like the case for the dielectric waveguide. At higher values of ν the collapse threshold falls off from the bulk prediction. The reason the collapse threshold for the beams in the metallic waveguide are closer to that of in the bulk, is that the power is that at the beginning of the simulation. In the dielectric waveguide, very little energy was lost on propagation. For the hollow metallic waveguide and capillaries, there is energy lost, so that the combination of loss and the necklace beam profile results in the threshold for collapse being above that of a radially symmetric beam.

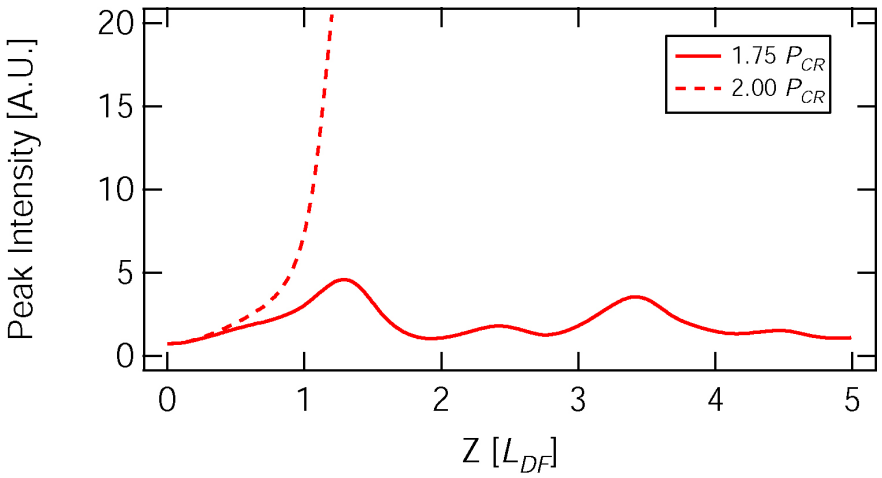


Figure 3.11 The peak intensity for the propagation of unperturbed $LP_{11}$ mode in a hollow metallic waveguide.

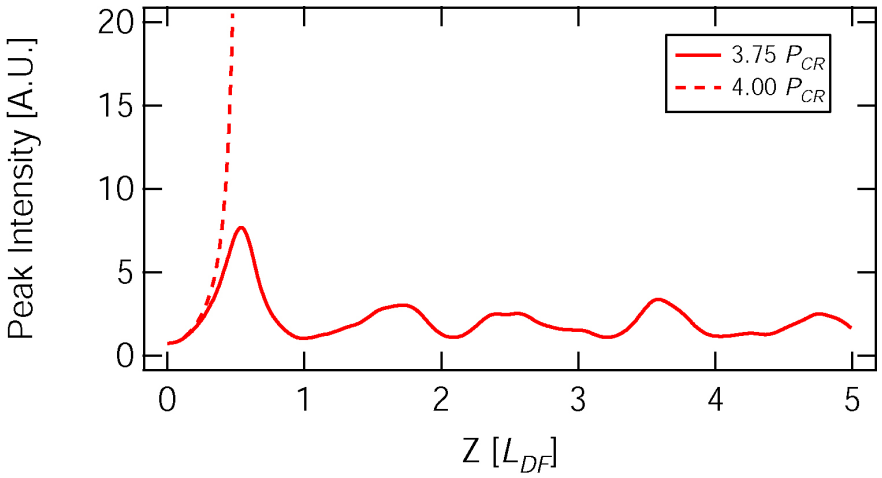


Figure 3.12 The peak intensity for the propagation of unperturbed $LP_{21}$ mode in a hollow metallic waveguide.

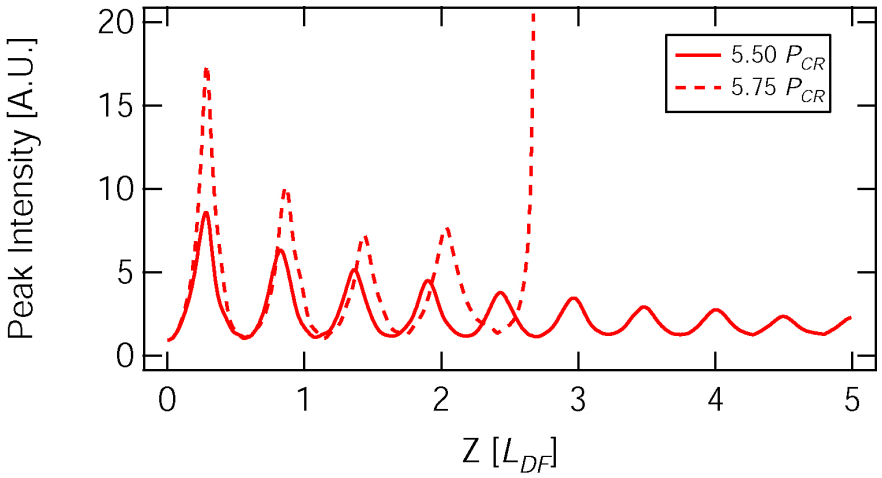


Figure 3.13 The peak intensity for the propagation of unperturbed $LP_{31}$ mode in a hollow metallic waveguide.

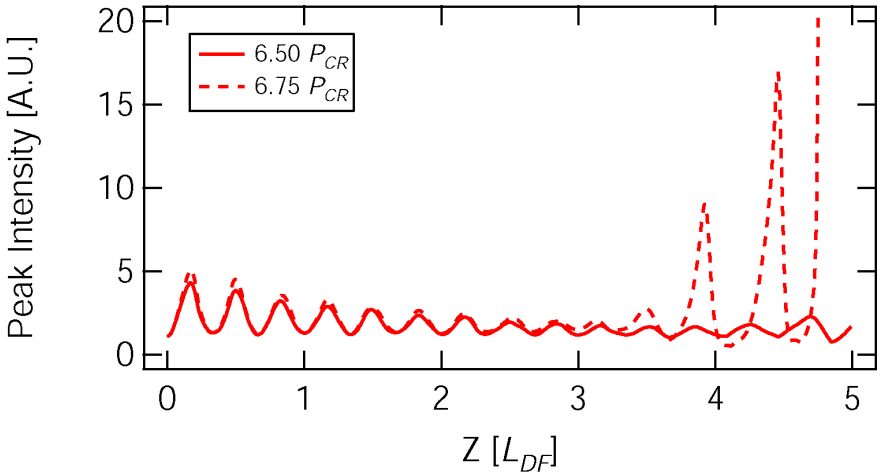


Figure 3.14 The peak intensity for the propagation of unperturbed $LP_{41}$ mode in a hollow metallic waveguide.

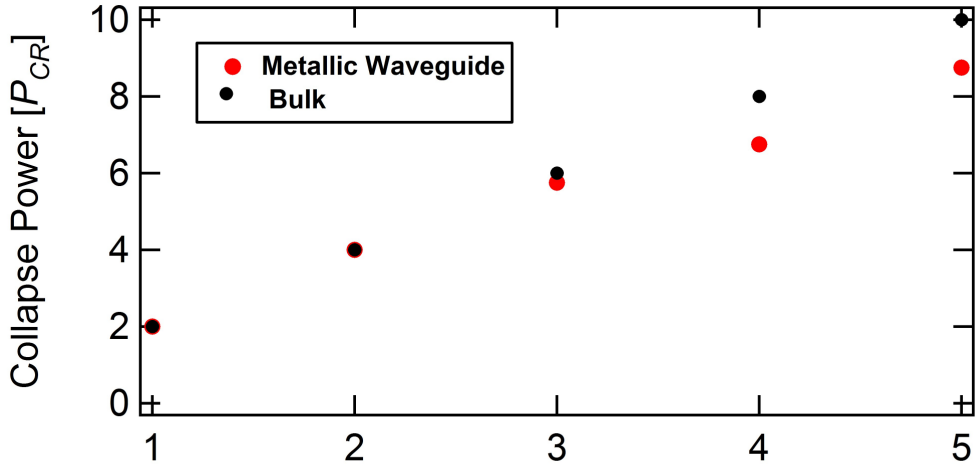


Figure 3.15 Collapse threshold as a function of ν for $LP_{\nu 1}$ modes in a hollow metallic waveguide.

### *3.4 Conclusions*

We see an increase in collapse threshold of the $LP_{\nu 1}$ over the radially symmetric fundamental mode in the fibers and hollow metallic waveguides over the distances studied. Similar to the studies done previously looking at the propagation of $LP_{\nu 1}$ modes with low values of ν, we find that there is an increase in the threshold power for collapse [6]. Further, we see a saturation effect in the threshold for collapse for higher values of ν in both dielectric waveguides and a

hollow metallic waveguide. Further, for the case of the dielectric waveguide, we find that the size of the waveguide does not have a large effect on the nonlinear propagation, it seems to be primarily the beaded structure of the necklace-like $LP_{v1}$ modes. In addition to this, there is also an increase in the self-focusing length, which is something suggested for ultra-large-mode-area-fibers [10]. The other important feature is that the beam profile retains the beaded structure for powers such as for 4.00 $P_{CR}$ for the $LP_{31}$ input. In addition, the importance of exciting a specific mode in the dielectric waveguide is shown, with small perturbations decreasing the threshold and collapse distance. These results help to advance the design and development of waveguide structures for the propagation of beams with powers above the critical power in dielectric and hollow structures.

REFERENCES


1. R.Y. Chiao, E. Garmire, and C.H. Townes, "Self-Trapping of Optical Beams," Phys. Rev. Lett. **13**, 479-482 (1964).

2. H.A. Haus, "Higher Order Trapped Light Beam Solutions," Appl. Phys. Lett. **8**, 128-129 (1966).

3. G. Fibich and A.L. Gaeta, "Critical power for self-focusing in bulk media and in hollow waveguides," Opt. Lett. **25**, 335-337 (2000).

4. K.D. Moll, A.L. Gaeta, and G. Fibich, "Self-Similar Optical Wave Collapse: Observation of the Townes Profile," Phys. Rev. Lett. **90**, 203902 (2003).

5. R.L. Farrow, D.A.V. Kilner, G.R. Hadley, and A.V. Smith, "Peak-power limits on fiber amplifiers imposed by self-focusing," Opt. Lett. **31**, 3423-3425 (2006).

6. G.R. Hadley, "High-Power Pulse Propagation in Optical Fibers," in *Optical Fiber Communication Conference/National Fiber Optics Engineers Conference,* OSA Technical Digest (CD) (Optical Society of America, 2008), paper OtuB1.

7. T. Pomintchev, M.C. Chen, D. Popmintchev, P. Arpin, S. Brown, S. Ališauskas, G. Andriukaitis, T. Balčiunas, O.D. Műcke, A. Pugzlys, A. Baltuška, B. Shim, S.E. Schrauth, A. Gaeta, C. Hernández-García, L. Plaja, A. Becker, A. Jaron-Becker, M.M. Murnane, H.C. Kapteyn, "Bright Coherent Ultrahigh Harmonic in the keV X-ray Regime from Mid-Infrared Femtosecond Lasers," Science **366**, 1287-1291 (2012).

8. G.R. Hadley and A.V. Smith, "Self-focusing in High-Power Optical Fibers," Proc. SPIE **6475**, 64750G (2007).

9. A.C. Peacock, P. Mehta, P. Horak, and N. Healy, "Nonlinear pulse dynamics in multimode silicon core optical fibers," Opt. Lett. **37**, 3351-3353 (2012).

10. H. Zhihua, W. Jianjun, L. Honghuan, X. Dangpeng, Z. Rui, L. Mingzhong, and W. Xiaofeng, "Self-focusing length in highly multimode ultra-large-mode-area fibers," Opt. Express **20**, 14604-14613 (2012).

11. A.D. Yablon and J. Jasapara, "Fiber designs for exceeding the bulk-media self-focusing threshold," Proc. SPIE **6543**, 64531D (2007).

12. S. Ramachandran, J.M. Fini, M. Mermelstein, J.W. Nicholson, S. Ghalmi, and M.F. Yan, "Ultra-large effective area, higher-order mode fibers: a new strategy for high-power lasers," Laser&Photon. Rev. **2**, 429-448 (2008).

13. J.W. Nicholson, J.M. Fini, A.M. Desantolo, X. Liu, K. Feder, P.S. Westbrook, V.R. Supradeepa, E. Monberg, F. DiMarcello, R. Ortiz, C. Headley, and D.J. DiGiovanni, "Scaling the effective area of higher-order-mode erbium-doped fiber amplifiers," Opt. Express **20**, 24575-24584 (2012).

14. D.A. Rockwell, V. Shkunov, and J.R. Marciante, "Semi-guiding high-aspect ratio core (SHARC) fiber providing single-mode operation and an ultra-large core area in a compact coilable package," Opt. Express **19**, 14746-14762 (2011).

15. D. Drachenberg, M. Messerly, P. Pax, A. Sridharan, J. Tassano and J. Dawson, "First multi-watt fiber oscillator in a high order mode," **21**, 18089-18096 (2013).

16. C.R. Giuliano, J.H. Marburger, and A. Yariv, "Enhancement of the self-focusing threshold in sapphire with elliptical beams," Appl. Phys. Lett **21**, 58-60 (1967).

17. G. Fibich and B. Ilan, "Self-focusing of elliptic beams: an example of the failure of the aberrationless approximation," J. Opt. Soc. Am. B **17**, 1749-1758 (2000).

18. M. Soljačić and M. Segev, "Self-trapping of "Necklace Beams" in Self-Focusing Kerr Media," Phys. Rev. Lett. **81**, 4851-4854 (1998).

19. M. Soljačić and M. Segev, "Self-trapping of "necklace-ring" beams in self-focusing Kerr media," Phys. Rev. E **62**, 2810-2820 (2000).

20. M. Soljačić and M. Segev, "Integer and Fractional Angular Momentum Borne on Self-Trapped Necklace-Ring Beams," Phys. Rev. Lett. **86**, 420-423 (2001).

21. T.D. Grow, A.A. Ishaaya, L.T. Vuong, and A.L. Gaeta, "Collapse and Stability of Necklace Beams in Kerr Media," Phys. Rev. Lett. **99**, 133902 (2007).

22. A.A. Ishaaya, T.D. Grow, S. Ghosh, L.T. Vuong, and A.L. Gaeta, "Self-focusing dynamics of coupled optical beams," Phys. Rev. A **75**, 023813 (2007).

23. W.Q. Thornburg, B.J. Corrado, and X.D. Zhu, "Selective launching of higher-order modes into an optical fiber with an optical phase shifter," Opt. Lett. **19**, 454-456 (1994).

24. W. Mohammed, M. Pichumani, A. Mehta, and E.G. Johnson, "Selective excitation of the $LP_{11}$ mode in step index fiber using a phase mask," Opt. Eng. **45**, 074602 (2006).

25. Y. Yan, L. Zhang, J. Wang, J.Y. Yang, I.M. Fazal, N. Ahmed, A.E. Willner, and S.J. Dolinar, "Fiber structure to convert a Gaussian beam to a higher-order optical orbital angular momentum modes," Opt. Lett. **37**, 3294-3296 (2012).

26. C. Pollock, *Fundamentals of Optoelectronics* (CBLS, 2003).

27. G.P. Agrwal, *Nonlinear Fiber Optics* (Academic Press, 2005).

# CHAPTER 4

## SPIRAL MOTION OF COLLAPSING BEAMS IN WATER

The interaction between light beams has been of significant interest, specifically the ability to control light beams from a distance. The interaction of solitons is one such related field, which has been extensively studied [1-11]. These studies have revealed a wealth of interesting phenomena related to the interactions of solitons, such as fusion, fission, annihilation, and stable orbiting. The specific propagation characteristics and the interactions between the solitons are generally set by the initial phase relationship between the solitons. These interactions have been studied in a wide range of materials, such as bulk quadratic media [4], photorefractive crystals [5,6], saturable nonlinear media [7,8], and nonlocal nonlinear media [9]. Some of the interest in the spiralling of solitons can be attributed to the properties of angular momentum as it relates to solitons. This could either be for general interest in angular momentum, or interest in the propagation dynamics of solitons with angular momentum [10], or the possibility of suppressing collapse of high power beams [11]. Such studies have provided a wealth of understanding on the behavior of solitons.

In a similar vein of study, the interaction between collapsing beams propagating in glass with a defined phase relationship has also been studied [12, 13]. These studies were carried out with the two beams travelling in one plane, so the only phenomena seen were attraction, repulsion, or fusion. Whether the beams were attracted to each other or repelled from each other was dependent on the initial phase. Whether the beams fused was dependent on the initial separation as well. Similar to the studies on solitions, these studies have expanded the understanding of interactions between collapsing beams in solids.

Recently the interest in the interaction of filaments has grown in the laser filamentation science community. The control of filaments at long distances is of great interest, hence the extension of these studies to the filamentation science field [14-16]. The interaction of filaments

in air was numerically studied and was shown to exhibit behavior similar to that of solitons and collapsing beams such as attraction, repulsion, fusion, energy transfer, and spiralling [14]. Experimental studies with small crossing angles have shown the deflection of time-overlapped filaments, though it was only about 7 degrees [15]. Energy exchange between two filaments with a larger crossing angle of 17 degrees has also been shown experimentally [16]. We continue along this vein of research and display large rotations of interacting, collapsing beams in water in an effort to further understand the interactions of collapsing beams.

### *4.1 Experimental setup*

The experimental setup is shown in figure 1. For the experiment we used an amplified Titanium:sapphire laser with center wavelength of 800 nm, a repetition rate of 1 kHz, and a 50 fs FWHM pulse width when optimally compressed. The output of the laser was spatially filtered and resized. After resizing, the beam was separated by a polarizing beam splitter into an s-polarized arm and a p-polarized arm. The s-polarized arm had a delay line. To control the phase relationship between the two arms, there was a computer controlled, motorized delay stage in the s-polarization arm. In the p-polarization arm there is a half-wave plate to rotate the polarization to s-polarization, so that there will be interaction between the beams in the water cell. The beams are recombined on a non-polarizing beam splitter. The beams are arranged in such a way that there is a vertical separation of 250 μm between the two beams, which remains constant for large time separation. There is also a horizontal separation, but the beams are arranged to cross with a very small angle in the water cell. The half-angle of the crossing is 0.063°. The beams start out separated at the beginning of an extendable water cell. The input and output windows of the cell are AR coated for 800 nm. The beams cross a distance 17.9 cm from the input

window of the water cell. The two beams have waists of approximately 180 μm, which means a diffraction length of approximately 17 cm. The water cell has a maximum length of 22.50 cm. The temporal characteristics of the input pulses at the beginning of the water cell are also of importance. The pulses are chirped at the input of the water cell, with FWHM pulse duration of 330 fs. This is done so that upon propagation in the water cell, the pulses compress. That way the highest intensity is at the interaction region, where the beams are crossing. Water has a group-velocity dispersion of 250 $fs^2$/cm. The dispersion length of a pulse has a FWHM pulse width of 50 fs in water is 3.6 cm.

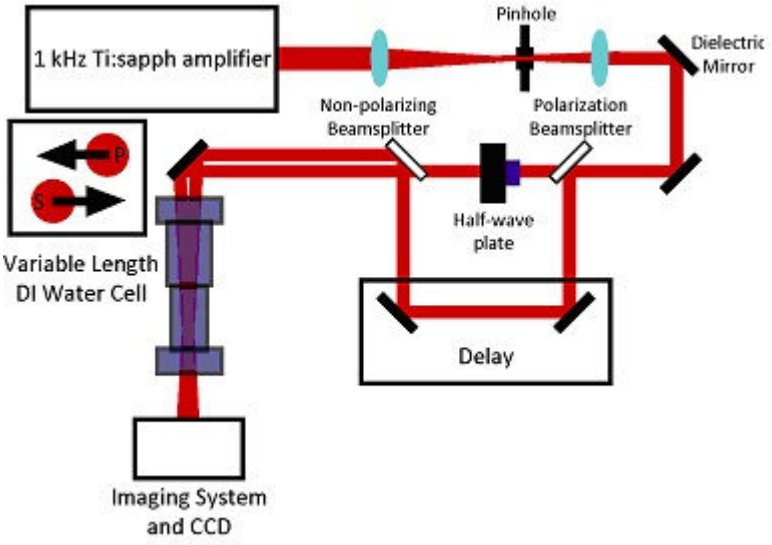


Figure 4.1 Experimental setup. The output of the laser is spatially filtered and resized. The beam is split by a polarizing beam splitter into a P-polarized arm and an S-polarized beam. The half wave plate in the P-arm rotates the polarization to S. There is a delay stage in the S-arm to vary the phase difference between the two beams. The two beams are then recombined on a non-polarizing beam splitter. The beams are not perfectly overlapped on the beam splitter. There is a constant vertical separation and a slight difference in k-vectors, resulting in a small crossing angle in the water cell. The inset shows the geometry of the beam profile at the input face of the extendable water cell.

Due to the construction of the water cell, the smallest propagation length at which we can measure the beam profiles is 16.5 cm from the input face of the water cell. This is just before the crossing point of the beams in the water cell, so there will be some interaction between the beams before this point as the beams move closer together. We are able to see the beam profiles right after the low power crossing point.

### *4.2 Experimental results*

Figure 4.2 shows the beam profiles for the case where each beam has energy of 4.20 μJ. The angle of rotation is determined by connecting the center of each beam, then using a simple geometric construction to determine the apparent angle of rotation. When the collapsing beams are separated (4 ps) in time, they propagate without interacting. Note that there does appear to

be an angle of rotation, but it is not rotation due to the interaction of the beams. The apparent angles are just due to the geometric construction, since the vertical separation remains the same. The horizontal separation on the other had increases due to the crossing geometry. As we look at beam profiles further along the propagation distance, we see the horizontal separation increase even for the case of no interactions between collapsing beams. For the case where they are overlapped in time, we see more rotation than would be expected to due to the simple crossing geometry. The interaction is evident in the change in the vertical separation between the two beams. The maximum rotation seen for these parameters is 32.66 degrees.

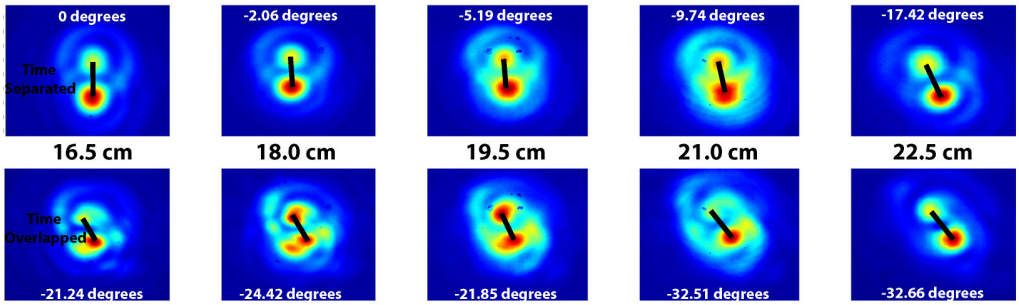


Figure 4.2 Beam profiles along propagation in the water cell for the case where both the S-arm and the P-arm have pulse energies of 4.20 μJ. The top row is the beam profiles for the time-separated case when the beams are not interacting, the bottom row is for interacting, time overlapped case.

We see the rotation in the very first beam profile and continue to see a greater rotation in each beam profile when compared to the non-interacting case, which does not show any change in the vertical separation between the two beams.

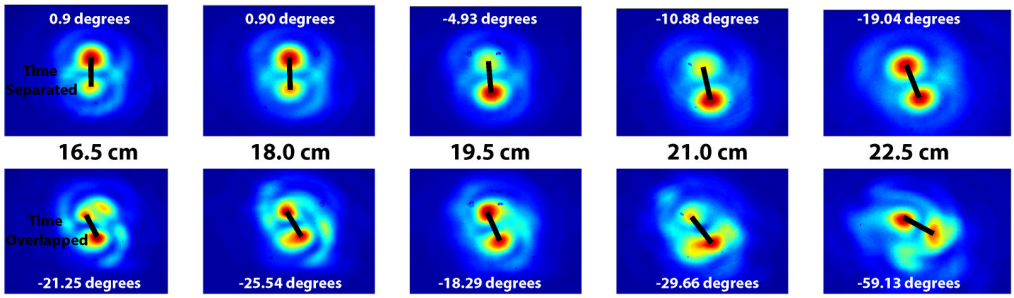


Figure 4.3 Beam profiles along propagation in the water cell for the case where both the S-arm and the P-arm have pulse energies of 4.90 μJ. The top row is the beam profiles for the time-separated case when the beams are not interacting, the bottom row is for interacting, time overlapped case.

As another example of this rotation, we increase the pulse energy in each arm to 4.90 μJ. The beam profiles for this larger input energy are shown in Figure 4.3. The non-interacting, time separated case is shown on the top row, while the interacting, time overlapped case is shown along the bottom. Again, we see rotation take place, with a maximum rotation of 59 degrees. This rotation can be seen clearly in the Figure 4.4, which shows the isosurface along the propagation length for the non-interacting A and interacting case B, respectively. The surface is the surface where the intensity is one-half that of the peak intensity. For the non-interacting case, the beams cross and continue to propagate in their original directions. For the interacting case, the rotation is easily seen, especially at the longest propagation distance. At the end of the water cell, we see rotation of 50 degrees, which is a difference of about 40 degrees from the non-interacting case. This is much greater than the previous experimental rotation of 7 degrees shown in air [15].

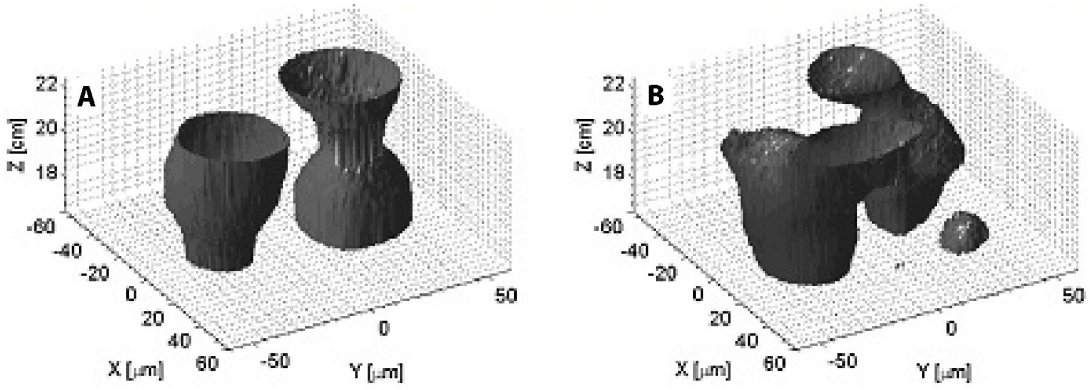


Figure 4.4 Isosurface for the 4.90 μJ input beam energy for the A. time separated case and for the B. time overlapped case.

Finally, we increase the input pulse energy to 5.30 μJ to see how the rotation changes with higher energy. Beam profiles for this higher energy are shown in figure 4.5. For these beam parameters, we see a maximum rotation of 50.23 degrees.

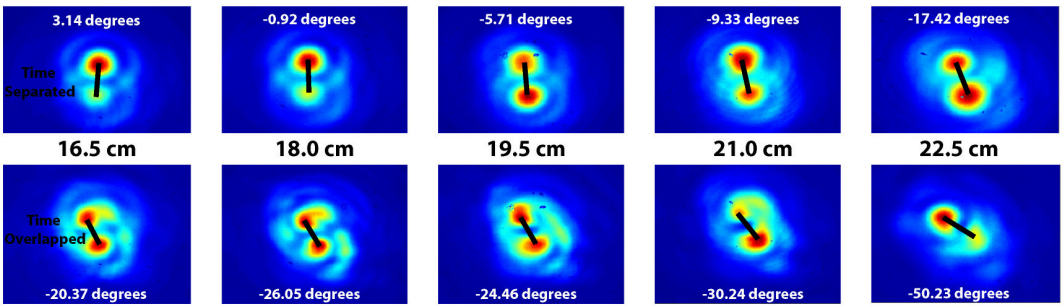


Figure 4.5 Beam profiles along propagation in the water cell for the case where both the S-arm and the P-arm have pulse energies of 5.30 μJ. The top row is the beam profiles for the time-separated case when the beams are not interacting, the bottom row is for interacting, time overlapped case.

The rotations for different energy levels are shown in figure 4.6. There are two interesting trends that can be gleaned from these results. The first trend is the large difference in rotation between the time-separated and time-overlapped cases. The interacting beams rotate 20-40 degrees more than the non-interacting case, which doesn't truly rotate. The apparent angle is just due to the horizontal beam separation increasing upon propagation. The second trend is the difference at long propagation lengths for the higher powers when the two beams are time-overlapped. For the time-separated case we measured the beam profiles at five different propagation distances for 3 different powers. As expected, the beams propagated without

rotation. This was expected, since there would be no interaction due to the instantaneous Kerr effect since there is a large (4ps) time separation. For the time-overlapped case, we see a marked difference when compared to the time-separated case. The beams have already crossed by the time they reached the geometric crossing point, so there has been interaction before the crossing point, which is to be expected. As the beams are propagating the separation between the beams is getting smaller due to the change in horizontal separation. The interaction of collapsing beams was shown to be heavily dependent on the separation of the beams [12]. As the beams get closer together, the interaction gets stronger. Since the beams are in phase with each other, this will be an attractive interaction. The attractive interaction is balanced by the difference in the propagation directions. The results in the large rotation we see in the beam profiles, showing a maximum rotation of 40 degrees when compared to the non-interacting case. The other interesting thing to note is the difference between the maximum rotation for the energies of 4.30 μJ, 4.90 μJ, and 5.30 μJ. The time-overlapped propagation with energy of 4.30 μJ shows smaller rotation then the both 4.90 μJ and 5.30 μJ. The interesting part is that the rotation for the 4.90 μJ is larger than that of the 5.30 μJ. We suspect this could be due to the Loss of Phase effect for collapsing beams [17].

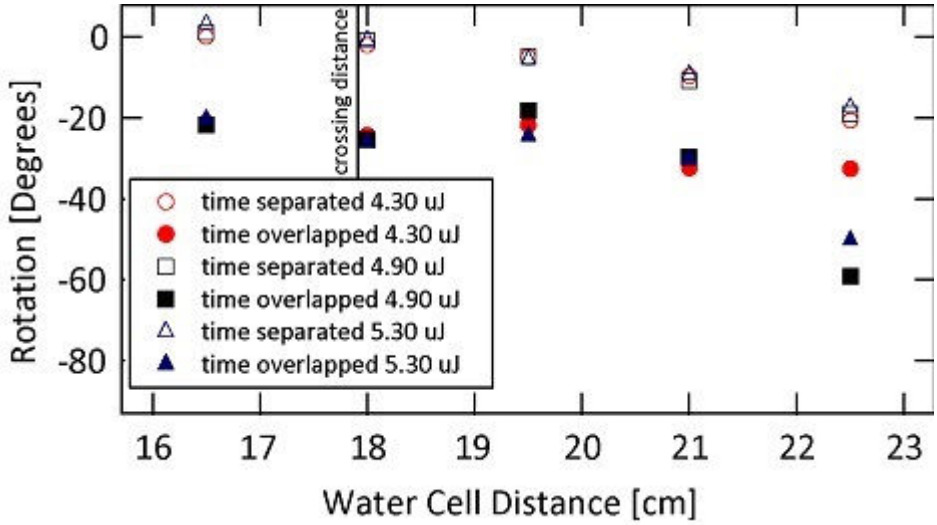


Figure 4.6 The apparent rotation seen for 3 different beam energies. For each energy, there are two cases, the time-separated case show the propagation dynamics when there is no interaction between the beams. The time-overlapped is when the beams are interacting with each other upon propagation. The difference between in apparent rotation between the two cases is clear.

### *4.3 Conclusion*

In conclusion, we have shown the interaction between collapsing beams in water can result in the rotation of the collapsing beams. We have shown it to be a large rotation of close to 60 degrees, with the difference between apparent rotation of the non-interacting case and the interacting case being about 40 degrees. This can act as a model for studying filament interactions in water and other transparent media. Future studies, both numerical and experimental could be carried out with a focus on the temporal and spectral characteristics of the interacting beams. Variations of the initial temporal and spectral characteristics, such as temporal or spectral chirp or pulse shape, could alter the interactions that take place. Also of interest are the output temporal and spectral profiles of the interacting beams after propagation. These studies could offer more insight into the spatio-temporal collapse dynamics of interacting beams.

REFERENCES


1. G.I Steeman and M. Segev, "Optical Spatial Solitons and Their Interactions: Universality and Diversity," Science **286,** 1518-1522 (1999).

2. C. Rotschild, B. Alfassi, O. Cohen, and M. Segev, "Long-range interactions between optical solitons," Nat. Photonics **2,** 769-774 (2006).

3. M. Shalaby, F. Reynaud, and A. Barthelemy, "Experimental observation of spatial soliton interactions with a π/2 relative phase difference," Opt. Lett. **17,** 778-780 (1992).

4. V.V. Steblina, Y.S. Kivshar, and A.V. Buryak, "Scattering and spiraling of solitons in a bulk quadratic medium," Opt. Lett. **23,** 156-158 (1998).

5. M. Shih, M. Segev, and G. Salamo, "Three-Dimensional Spiraling of Interacting Spatial Solitons," Phys. Rev. Lett. **78,** 2551-2554 (1997).

6. Stepken, M.R. Belić, F. Kaiser, W. Królikowski, and B. Luther-Davies, "Three Dimensional Trajectories of Interacting Incoherent Photorefractive Solitons," Phys. Rev. Lett. **82,** 540-543 (1999).

7. V. Tikhonenko, J. Christou, B. Luther-Davies, "Three Dimensional Bright Spatial Soliton Collision and Fusian in a Saturable Nonlinear Medium," Phys. Rev. Lett. **76,** 2698-2701 (1996).

8. A.V. Buryak, Y.S. Kivshar, M. Shih, and M. Segev, "Induced Coherence and Stable Soliton Sprialing," Phys. Rev. Lett. **82,** 81-84 (1999).

9. D. Buccoliero, S. Lopez-Aguayo, S. Skupin, A.S. Desyatnikov, O. Bang, W. Krolikowski, Y.S. Kivshar, "Spiraling solitons and multipole localized modes in nonlocal nonlinear media," Physica B **394,** 351-356 (2007).

10. W.J. Firth and D.V. Skryabin, "Optical Solitons Carrying Orbital Angular Momentum," Phys. Rev. Lett. **79,** 2450-2453 (1997).

11. A.S. Desyatnikov, D. Buccoliero, M.R. Dennis, and Y.S. Kivshar, "Suppression of collapse for spiraling elliptic solitons," Phys. Rev. Lett. **104,** 053902 (2010).

12. A.A. Ishaaya, T.D. Grow, S. Ghosh, L.T. Vuong, and A.L. Gaeta, "Self-focusing dynamics of coupled optical beams," Phys. Rev. A **74,** 023813 (2007).

13. E. D'Asaro, S. Heidari-Bateni, A. Pasquazis, G. Assanto, J. Gonzalo, J. Solis, and C.N. Alfonso, "Interaction of self-trapped beams in high index glass," Opt. Exp. **17,** 17150-17155 (2009).

14. T.T. Xi, X. Lu, and J. Zhang, “Interaction of Light Filaments Generated by Femtosecond Laser Pulses in Air,” Phys. Rev. Lett. **96,** 025003 (2006).

15. B. Shim, S.E. Schrauth, C.J. Hensley, L.T Vuong, P. Hui, A.A. Ishaaya, and A.L. Gaeta, “Controlled interactions of femtosecond light filaments in air,” Phys. Rev. A **81,** 061803(R) (2010).

16. P. Ding, Z. Guo, X. Wang, Y. Cau. M. Sun, P. Zhao, Y. Shi, S. Sun, X. Liu, and B. Hu, “Energy exchange between two noncollinear filament-forming laser pulses in air,” Opt. Exp. **21,** 27631-27640 (2012).

17. B. Shim, S.E. Schrauth, A.L. Gaeta, M.K. Klein, and G. Fibich, “Loss of Phase of Collapsing Beams,” Phys. Rev. Lett. **108,** 043902 (2012).

# CHAPTER 5

# CONCLUSION AND FUTURE WORK

Here we have presented work exploring the nonlinear propagation of ultrashort pulses in transparent media, in which the initial conditions have significant effects on the dynamics. Tailoring these initial conditions for a desired result after propagation is fundamentally interesting, relevant, and useful. For example, it could be producing a specific temporal profile for a desired output as in the case of the super-Gaussian pulse collapse resulting in pulse-splitting as opposed to spatio-temporal collapse. Another case in which the initial conditions can change the dynamics is the choice of input profile. There is the possibility of using a non-Gaussian input in order to increase the collapse threshold and collapse distance as for the propagation of the higher-order necklace beams in waveguides. Finally, setting up the initial beams with a given phase difference, separation, and direction can produce interactions such as rotation upon self-focusing. All of these results further the understanding of the importance that initial conditions play in the self-focusing of ultrashort pulses in transparent media.

The study of super-Gaussian pulses in the anomalous-GVD regime is an example of experiments exploring spatio-temporal collapse dynamics by using the results of spatial collapse experiments. By using a 4-*f* shaper [1], the spatio-temporal collapse dynamics in the anomalous-GVD regime of materials can be studied in order to glean fundamental or applicable results. The spatio-temporal collapse of a spatial and temporal Super-Gaussian study is possibly of interest due to the possibility of observing pulse-splitting as the super-Gaussian pulse collapses and a spatial ring profile as the super-Gaussian spatial profile collapses. Also, using spatial experiments as a guide, the collapse and filamentation of high-power Airy-ring, also known as abruptly autofocusing beams, have been studied in the spatial domain with the goal of tailoring the filamentation properties, such as collapse [2]. Perhaps the autofocusing pulses would have interesting temporal dynamics upon self-focusing in the anomalous-GVD regime, perhaps

resulting in a single pulse in the temporal domain, much like the experiment in the spatial domain results in a localized beam. The demonstration of the super-Gaussian pulse not undergoing spatio-temporal collapse in the anomalous-GVD regime is important because it shows that other pulse-shapes may exhibit interesting and unexpected collapse dynamics in this regime.

In addition, the nonlinear geometrical optics (NGO) method succeeded in qualitatively reproducing the numerical and experimental results of a super-Gaussian pulse in the anomalous-GVD regime. The NGO method could be used to gain some intuition into the high-power collapse of a specific high-power temporal pulse shape, without the need for numerical integration [3]. This would be beneficial in the initial planning for experiments as a way to discover what pulse shapes would be interesting before devoting the full experimental and numerical resources to generating and simulating the desired pulse shape. Looking at self-focusing dynamics in the anomalous-GVD regime, specifically applying the NGO method, for high-power pulses allows for new temporal dynamics to be discovered from spatial results.

The high-power propagation of the necklace higher-order modes in fibers are relevant to many experiments related to high-power propagation in waveguides, both hollow and dielectric. The propagation in dielectric waveguides could be of use in pursuing the development of high-power fiber lasers and amplifiers, similar to what has been done with previous large mode area fibers, both radially symmetric [4, 5], and more specialized fibers such as high aspect ratio rectangular core fibers [6, 7]. In addition, if there is the possibility of designing and fabricating specific optical fiber, the combination of a designed fiber and propagation of a higher-order might further increase collapse thresholds in dielectric fibers. The large hollow capillaries are applicable to studies of nonlinear interactions in gas filled capillaries for such as high-harmonic generation [8]. The higher-order modes could allow for higher power beams to be sent through the hollow, gas-filled waveguide. It could also be interesting to generate high-harmonics in a necklace shape as opposed to something approximating a Gaussian beam profile. Higher-order modes that have a necklace shape can be of use in further studies of high-power optical pulse

propagation through waveguides, whether they are dielectric or hollow, for such things as lasers and nonlinear interactions with gas. As this work was numerical, the next step is to try and experimentally verify the propagation dynamics of these necklace type modes in fiber.

The interaction of beams that resulted in the observation of spiral motion in water is important from both a fundamental and application point of view. Many of the studies in filamentation science have been interested in the control of filaments at a distance [9, 10]. The Airy-ring beams are one example of this theoretical and experimental interest in how spatial input profile can affect the collapse and filamentation dynamics. The spatial profile of the initial beam is tailored to give a desired result upon nonlinear propagation [2]. In this case it was intended to generate a filament at a specific distance. Another possible extension of the interaction of collapsing beams is looking at the interactions of more than two beams with different phases and propagation directions. The study of the spiral motion of collapsing beams in water adds to the field of interaction of collapsing beams.

Another future direction involves modeling the spatio-temporal dynamics of the interacting collapsing beams. This would build off of the spatio-temopral super-Gaussian pulse collapse dynamics and the interacting beams. The possibility of setting up interacting beams with non-Gaussian pulse shapes would be interesting. Not only would looking at how the initial pulse shape changes the interaction upon propagation be interesting, also looking at how the initial pulse shape itself changes upon propagation would be interesting.

We have demonstrated the importance that the initial conditions of a self-focusing laser beam or beams can have on the self-focusing dynamics upon propagation in a transparent medium. This work gives further insight into the ways in which the initial conditions of collapsing laser beams can alter collapse dynamics. It is applicable to such fields as nonlinear beam collapse, high-power propagation in fiber, and filamentation studies in condescended media and gases. Future studies are promising to expand on this work and contribute to these fields.

REFERENCE


1. A.M. Weiner, J.P. Heritage, and E.M. Kirschner, "High-resolution femtosecond pulse shaping," J. Opt. Soc. Am. B **5**, 1563-1572 (1998).

2. P. Panagiotopoulos, D.G. Papazoglou, A. Couairon, and S. Tzortzakis, "Sharply autofocused ring-Airy beams transforming into non-linear intensie light bullets," Nat. Commun. **4**, 2622 (2013).

3. N. Gavish, G. Fibich, L.T. Vuong, and A.L. Gaeta, "Predicting the filamentation of high-power beams and pulses without numerical integration: A nonlinear geometrical optics method," Phys. Rev. A **78**, 043807 (2008).

4. S. Ramachandran, J.M. Fini, M. Mermelstein, J.W. Nicholson, S. Ghalmi, and M.F. Yan, "Ultra-large effective area, higher-order mode fibers: a new strategy for high-power lasers," Laser&Photon. Rev. **2**, 429-448 (2008).

5. J.W. Nicholson, J.M. Fini, A.M. Desantolo, X. Liu, K. Feder, P.S. Westbrook, V.R. Supradeepa, E. Monberg, F. DiMarcello, R. Ortiz, C. Headley, and D.J. DiGiovanni, "Scaling the effective area of higher-order-mode erbium-doped fiber amplifiers," Opt. Express **20**, 24575-24584 (2012).

6. D.A. Rockwell, V. Shkunov, and J.R. Marciante, "Semi-guiding high-aspect ratio core (SHARC) fiber providing single-mode operation and an ultra-large core area in a compact coilable package," Opt. Express **19**, 14746-14762 (2011).

7. D. Drachenberg, M. Messerly, P. Pax, A. Sridharan, J. Tassano and J. Dawson, "First multi-watt fiber oscillator in a high order mode," **21**, 18089-18096 (2013).

8. T. Pomintchev, M.C. Chen, D. Popmintchev, P. Arpin, S. Brown, S. Ališauskas, G. Andriukaitis, T. Balčiunas, O.D. Műcke, A. Pugzlys, A. Baltuška, B. Shim, S.E. Schrauth, A. Gaeta, C. Hernández-García, L. Plaja, A. Becker, A. Jaron-Becker, M.M. Murnane, H.C. Kapteyn, "Bright Coherent Ultrahigh Harmonic in the keV X-ray Regime from Mid-Infrared Femtosecond Lasers," Science **366**, 1287-1291 (2012).

9. A. Couairon and A. Mysyrowicz, "Femtosecond filamentation in transparent media," Phys. Rep., **441**, 47 (2007).

10. G. Fibich, Y. Sivan, Y. Ehrlich, E. Louzon, M. Fraenkel, S. Eisenmann, and A. Zigler, "Control of collapse distance in atmospheric propagation," Opt. Express **14**, 4946-4957 (2006).